Advances in Physics: X

ISSN: (Print) (Online) Journal homepage: https://www.tandfonline.com/loi/tapx20

State-to-state dissociative photoionization of molecular nitrogen: the full story

T. Ayari , M. Desouter-Lecomte , R. Linguerri , G. A. Garcia , L. Nahon , A. Ben Houria , H. Ghalila , R. Ben Said & M. Hochlaf

To cite this article: T. Ayari , M. Desouter-Lecomte , R. Linguerri , G. A. Garcia , L. Nahon , A. Ben Houria , H. Ghalila , R. Ben Said & M. Hochlaf (2020) State-to-state dissociative photoionization of molecular nitrogen: the full story, Advances in Physics: X, 5:1, 1831955, DOI: 10.1080/23746149.2020.1831955

To link to this article: https://doi.org/10.1080/23746149.2020.1831955

Published online: 23 Oct 2020.

ADVANCES IN PHYSICS: X
2020, VOL. 5, NO. 1, 1831955
https://doi.org/10.1080/23746149.2020.1831955

Taylor & Francis
Taylor & Francis Group

REVIEW

OPEN ACCESS Check for updates

State-to-state dissociative photoionization of molecular nitrogen: the full story

T. Ayari[a,b], M. Desouter-Lecomte[c], R. Linguerri[a], G. A. Garcia[d], L. Nahon[d], A. Ben Houria[b], H. Ghalila[b], R. Ben Said[e] and M. Hochlaf[a]

[a]COSYS/LISIS, Université Gustave Eiffel, Champs-sur-Marne, France; [b]Laboratoire De Spectroscopie Atomique, Moléculaire Et Applications – LSAMA, Université De Tunis El Manar, Tunis, Tunisia; [c]Institut De Chimie Physique, UMR8000, Université Paris-Saclay, CNRS, Orsay, France; [d]Synchrotron SOLEIL, L'orme Des Merisiers, Saint-Aubin, Gif-sur-Yvette Cedex, France; [e]Department of Chemistry, College of Science and Arts, Qassim University, Ar Rass, Saudi Arabia

ABSTRACT

N_2 is a major constituent of Earth and planetary atmospheres. First, evidenced in 1952, the dissociative photoionization of molecular nitrogen, N_2, plays an important role in the species abundance, out of equilibrium evolution, and chemical reactivity of diverse media including upper atmospheres (the so-called ionospheres) and plasma. Many scenarios were proposed for rationalizing the dissociative ionization mechanisms and exit channels, which are reviewed here, mainly involving the N_2^+ ($C^2\Sigma_u^+$, v^+) vibrational levels state-to-state dynamics on which we focus. We show, however, that previous studies are not comprehensive enough for fully shedding light on the complex undergoing processes. As a complementary global work, we used state-of-the-art quantum chemistry, time dependent and independent theoretical approaches associated to advanced experimental techniques to study the unimolecular decomposition of the N_2^+ ions forming the N^+ + N products. In addition to the already suggested spin-orbit-induced predissociation of the cationic $C^2\Sigma_u^+$ state, we documented a new mechanism based on vibronic coupling and tunneling dissociation. Besides, the quantum processes highlighted here should be also in action in the dynamics of electronically excited larger molecular systems involved in physical and chemical phenomena in plasma and in various natural environments on Earth and beyond.

ARTICLE HISTORY
Received 20 May 2020
Accepted 29 September 2020

KEYWORDS
Molecular nitrogen; photoionization; *ab initio* computations; dynamical computations; state-to-state reactions

CONTACT M. Hochlaf hochlaf@univ-mlv.fr COSYS/LISIS, Université Gustave Eiffel, Champs-sur-Marne, 77454, France

Presently at Department of Physics, Khalifa University, P.O. Box 127788, Abu Dhabi, United Arab Emirates

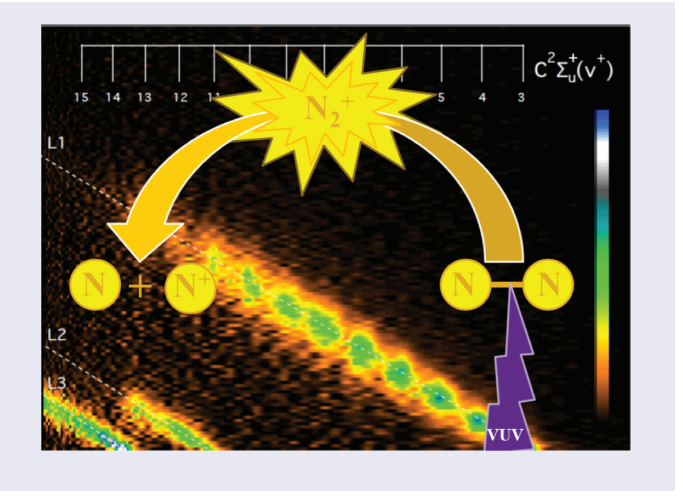

I. Introduction

The dissociative photoionization of molecular nitrogen, N_2, plays an important role in diverse media such as the upper Earth's atmosphere (ionospheres), in planetary atmospheres, in astrophysical media (interstellar medium) and in plasma. Indeed, atomic and molecular nitrogen and their ions are important species in planetary science and astrophysics because of the relatively large N_2/H_2 universal abundance ratio of 1.6×10^{-4}. In particular, molecular nitrogen is a major constituent of Earth's atmosphere [1] and of the upper atmospheres of Jupiter, Saturn and its largest moon Titan [2,3,4]. It protects the Earth from high-energy vacuum ultraviolet (VUV) and extreme ultraviolet (XUV) radiations and plays a major role in the chemistry of the thermosphere [5,6]. The photochemistry of N_2 in a variety of environments, e.g., the interstellar medium, extrasolar planets, and circumstellar envelops is believed to be responsible for the synthesis of N-containing molecules, including prebiotic molecules (e.g., HCN, CH_3CN) [7–9], which are precursors of larger molecules such as the building blocks of life [10–12], and also triggers the formation of N-containing aerosols such as those found in Titan's atmosphere [13].

VUV and XUV radiations interacting with neutral N_2 lead to its ionization and its dissociative ionization to form N_2^+ and $N + N^+$, respectively. In addition, the neutral dissociation of N_2 by absorbing VUV light produces excited N radical atoms and even excited N^+ ions [14,15,16]. These processes take place, for instance, in Earth's upper atmosphere after absorption of the solar radiation in the VUV and XUV ranges [17]. They occur along the potential energy curves (PECs) of the electronic-excited states of the N_2^+ cation, where both spin-orbit and

nonadiabatic relaxation phenomena are in action. N_2^+ is also formed in the bow shock wave found in front of heat shields during entry into the Earth's atmosphere. Moreover, it is suspected to be responsible for the escape of He^+ ions from the atmosphere after charge transfer collisions between N_2^+ and neutral He [18]. For the realistic modeling of these phenomena, one needs accurate descriptions of the electronic states of this ion and in-depth understanding of its formation and destruction dynamics via N_2 photo – and dissociative ionizations.

The dissociative photoionization of molecular nitrogen was evidenced for the first time in 1952. Since then, several scenarios were proposed in order to explain the formation of the N + N^+ fragments following the predissociation of the cation. These works are reviewed in Section 2. However, we will show, that the various involved processes are complex and cannot be understood within a single picture. At present, we performed complementary experimental works on the single photon ionization of N_2 using synchrotron VUV light source coupled to advanced double imaging electron/ion coincidence detector. We investigated the dynamics of the N_2^+ cation on a newly computed set of N_2^+ PECs and their couplings using two well-established state-of-the-art theoretical methodologies. These up-to-date experimental and theoretical results complement those already available. The full examination of the processes that may occur upon formation of an N_2^+ ion reveals that, in addition to the already suggested spin-orbit-induced predissociation, which are in action for the low vibrational levels of the $N_2^+(C^2\Sigma_u^+)$ state, the upper levels correspond to resonances, which dissociation is documented here for the first time. In summary, we shed light on the complex dynamics undertaken by the N_2^+ ions forming the N^+ + N products, which remained not fully explained for more than 60 years. This work should help in understanding the state-to-state complex dynamics of electronically excited larger molecular systems relevant for astrophysics, planetary sciences and in plasma physics. Indeed, N_2^+ C state represents a prototype molecular system, where the observed features and processes are easily found in large molecules.

II. Overview on the dissociative ionization of N_2 via the $N_2^+(C^2\Sigma_u^+)$ state

Back in 1952, Douglas [19] observed a strong enhancement of the N_2^+ ($C^2\Sigma_u^+$, $v^+ = 3$) bands in a He + N_2 discharge. He showed that this is due to inverse predissociation, i.e. $N(^4S) + N^+(^3P) \rightarrow N_2^+(C^2\Sigma_u^+)$, where the N^+ ions are produced via charge transfer reactions involving the He^+ ions. In 1959, Carroll [20] documented the direct predissociation of the C state to form N^+ + N, which occurs in the vicinity of the $v^+ = 3$ level. Since then, a multitude of experimental and theoretical

works were devoted to the identification of the mechanism(s) responsible for this predissociation. Indeed, the production of N^+ ions was studied using mass spectrometry [21–24]. The $N_2^+(C^2\Sigma_u^+)$ ions are also characterized to be long-lived enough to fluoresce and hence are responsible for the second negative system of N_2^+ (i.e. the $C^2\Sigma_u^+$–$X^2\Sigma_g^+$ emission transition). In the early seventies, Wankenne and Momigny [21] determined a lifetime of 0.8 μs for the $N_2^+(C^2\Sigma_u^+)$ ion before radiationless decomposition. However, a much shorter radiative lifetime ($\tau(v^+ \leq 2) = 0.09$ μs) was deduced by Govers and co-workers [24,25] using either electron or ion impact-induced $N_2^+(C^2\Sigma_u^+)$ predissociation. In 1976, Erman [26] rationalized both observations after direct measurement of the lifetimes of the $N_2^+(C^2\Sigma_u^+, v^+ = 1–5)$ vibrational levels using high-resolution high-frequency deflection technique. He determined a radiative lifetime of 78.9 ±3.0 ns for $v^+ = 2$ level and lifetimes of 4–5 ns for $v^+ \geq 3$ and attributed the sharp drop of these lifetimes to the already noticed predissociation of the $v^+ \geq 3$ states populating the lowest dissociation limit, L1: $N(^4S) + N^+(^3P)$. The corresponding predissociation rate was measured ~2 x 10^8 s^{-1}. In 1974, Asbrink and Fridh [27] observed the population of the upper dissociation limits by dissociative ionization of N_2. Later on, the threshold photoelectron-photoion coincidence spectroscopic investigations of the valence and inner-valence states of N_2^+ by Nicolas *et al.* [28] and by Aoto *et al.* [29] measured the following branching ratios (BRs): BRs = 100% to the L1 limit for C state v^+ levels located in the energy range between L1 ($N^+(^3P) + N(^4S)$), and L2 ($N^+(^1D) + N(^4S)$); for those located between L2 and L3 ($N^+(^3P) + N(^2D)$), BRs ~ 60% to L1 and 40% to L2; and BRs ~ 100% to L3 for those located above L3. Recent experimental and theoretical investigation dealing with the dissociation dynamics of N_2^+ induced by isolated attosecond XUV pulses in combination with few-optical-cycle near-infrared/visible (NIR/VIS) pulses showed that most of the N_2^+ ions decay to populate L2 (BR = 77.1%) and L3 (BR = 14.0%) and to a lesser extent the following upper limit L4 (BR = 8.5%), whereas a 0% branching ratio is measured for L1 [30]. The use of higher energy XUV femtosecond light induces the population of the upper dissociation limits of N_2^+ [31]. In sum, different BRs are measured depending on the specific vibrational or electronic states of N_2^+ populated by ionizing $N_2(X^1\Sigma_g^+)$. Moreover, Govers and co-workers showed the existence of a large isotope effect on these predissociations [25,32–36]. All these findings are the signature of a complex dynamics undergone by the N_2^+ ions.

In the 24–28 eV energy domain above $N_2(X^1\Sigma_g^+, v" = 0)$, the formation of the $N^+ + N$ pair corresponding to the dissociation limits L1, L2 and L3 is ascribed to the predissociation of the $N_2^+(C^2\Sigma_u^+)$ state. The question of

which states are involved in such predissociation has been the subject of much discussions in the course of which several scenarios were suggested [26,28,37–44]. They can be gathered into two main mechanisms known as the 'direct' and the 'accidental' mechanisms. The direct predissociation involves the conversion into the continuum of the $N_2^+(B^2\Sigma_u^+)$ state either due to finite vibrational interaction or after crossing a repulsive state, or a repulsive part of an attractive state. On the other hand, the accidental predissociation starts by the population of a bound intermediate state, which is then predissociated by a second repulsive state. In both cases, the implication of the N_2^+ quartet states and their spin-orbit couplings with the neighboring doublets was invoked. Up-to-date, none of these mechanisms, however, fully explained the state-to-state dissociative photoionization of N_2 and the subsequent complex unimolecular decomposition dynamics undertaken by the $N_2^+(C^2\Sigma_u^+, v^+)$ ions.

III. On the potentials and couplings of the N_2^+ ion

a. Potential energy curves

The full interpretation of the state-to-state dissociative photoionization of N_2 requires the mapping of the PECs of all N_2^+ cationic electronic states correlating to L1, L2 and L3 and those electronic states correlating to the upper asymptotes lying in energy below 28 eV with respect to $N_2(X^1\Sigma_g^+, v'' = 0)$. We thus computed N_2^+ states of doublet, quartet, and sextet spin multiplicities in both *ungerade* and *gerade* symmetries. The electronic calculations were performed using the MOLPRO 2015 program suite [45] in the D_{2h} point group symmetry. We used the complete active space self-consistent field (CASSCF) [46,47] technique followed by the internally contracted multi-reference configuration interaction (MRCI) [48–50] approach. We described the nitrogen atom by a large basis set of aug-cc-pV5Z quality [51,52], which is augmented by 3s and 2p diffuse Gaussian-type orbitals (GTOs). This results in 254 contracted Gaussian functions, to be used. In CASSCF, the active space was composed of the valence molecular orbitals (MOs) of N_2^+ to which we added one σ_g and one π_g MOs for better relaxation of the wavefunctions of the N_2^+ electronic states whose configurations differ in their σ and π orbital occupations. We used an active space larger than the valence and a diffuse basis set for better description of the possible diffuse nature of the valence-Rydberg states of N_2^+ as discussed for neutral N_2 [53,54]. For MRCI calculations, all configurations in the CI expansion of the CASSCF wavefunctions were taken as a reference and all valence electrons were correlated. Hence, we considered more than 4.8×10^8 uncontracted configuration state functions per symmetry. Using these highly correlated wavefunctions, we deduced the radial, the rotational and

the spin-orbit couplings between the electronic states involved in the $C^2\Sigma_u^+$ state predissociation. The spin-orbit integrals were evaluated, in Cartesian coordinates, over the MRCI wavefunctions, where the effective Breit-Pauli SO operator, $\mathbf{H^{SO}}$, as implemented in MOLPRO was used [55].

The N_2^+ MRCI/aug-cc-pV5Z PECs are displayed in Figure 1. For the bound states, the respective potential energy curves were incorporated into nuclear motion treatments in order to deduce a set of spectroscopic constants for the N_2^+ states. Thus, we used the method of Cooley [63] and the derivatives at the minimum energy distances and standard perturbation theory. The corresponding data are listed in Table 1. This table lists the spectroscopic parameters of the bound states including their equilibrium distances, vibrational and rotational constants, and excitation energies. The comparison to the previous experimental and previous theoretical data shows an overall good agreement, asserting the good quality of our PECs. The pattern of the vibrational levels of the $C^2\Sigma_u^+$ state is also obtained using a variational treatment and time-dependent approach.

Figure 1 shows the high density of electronic states lying in the vicinity of the N_2^+ ($C^2\Sigma_u^+$) state that may participate to its direct or accidental predissociation mechanisms. Both of them require the couplings with the $N_2^+(C^2\Sigma_u^+)$ state either by vibronic or spin-orbit couplings and the subsequent mixings of their wavefunctions. Nevertheless, standard selection rules reveal that only *ungerade* electronic states are in action in the dissociative single photon ionization of N_2, ruling out the contribution of the *gerade* states in this energy domain. Moreover, only quartet electronic states correlate adiabatically to the second dissociation limit L2. Thus, their implication cannot be excluded for the formation of, at least, $N^+(^1D)$ + N products. Consequently, we present in Figures 2 and 3 the electronic states and their mutual couplings that are *a priori* participating to the formation of N + N^+ ions in the 24–28 eV energy domain.

Figure 2 shows that the adiabatic PEC of the $C^2\Sigma_u^+$ state exhibits two potential energy wells: the inner potential where we locate 14 vibrational levels and two quasi-bound shape resonances; and the outer potential that also accommodates several bound levels with a large interatomic equilibrium distance (see Section VI). Both potential wells are separated by a barrier due to the avoided crossing with the $3^2\Sigma_u^+$ state. At these large internuclear separations, the $C^2\Sigma_u^+$ state interacts with the $3^2\Sigma_u^+$ state by radial coupling (Figure 3(a)) and with the lower $B^2\Sigma_u^+$ state as discussed in Refs [43,44]. The shape of the radial coupling between the $C^2\Sigma_u^+$ and $3^2\Sigma_u^+$ states (Figure 3(a)) exhibits a maximum for NN distances between 3–3.5 bohr *i.e.* close to the maximum of the $C^2\Sigma_u^+$ state potential barrier due to the avoided crossing between both states. This indicates thus that the excited vibrational states of the $C^2\Sigma_u^+$ state are coupled with the $3^2\Sigma_u^+$. Although the vibronic eigenstates have always components on both electronic states (cf.

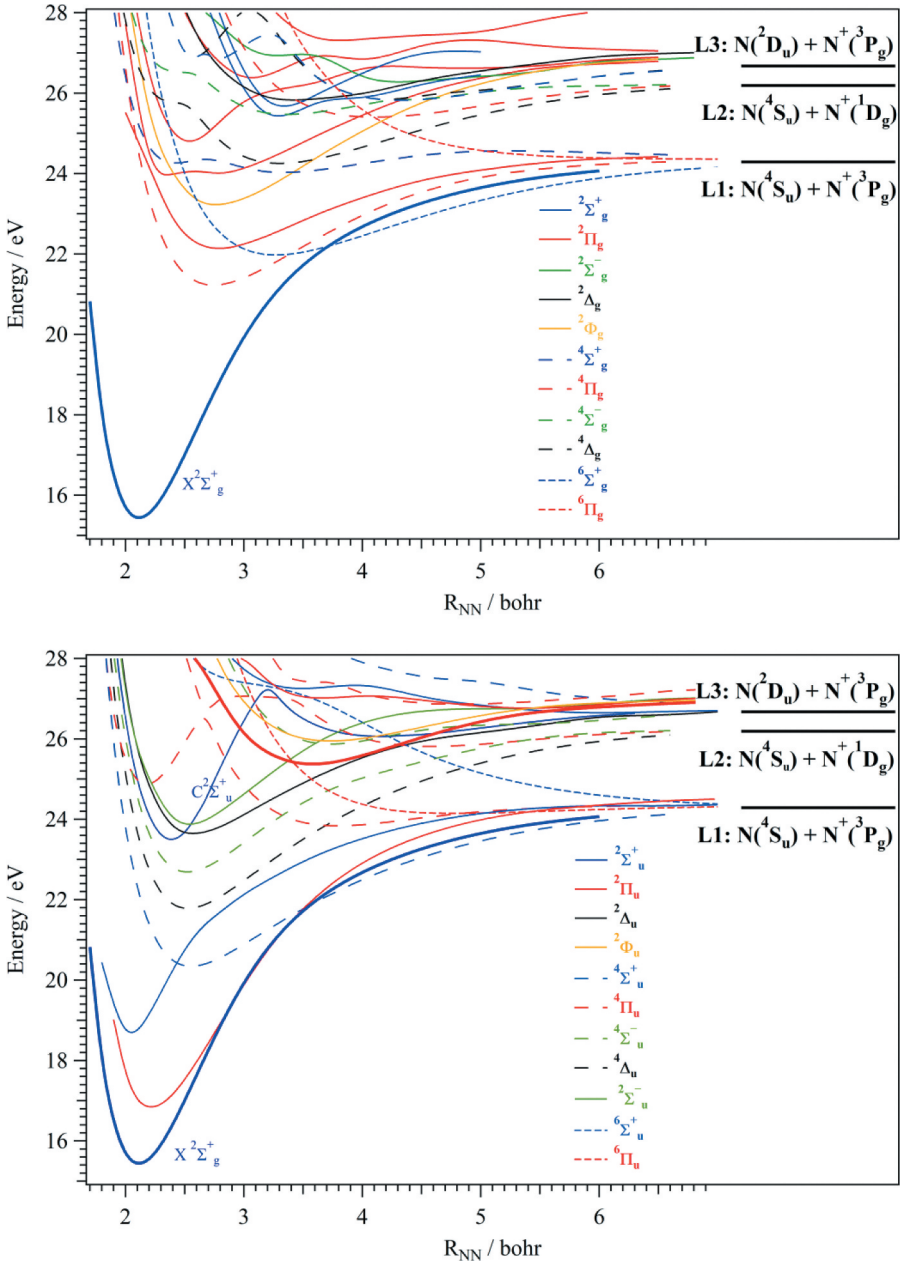

Figure 1. MRCI/aug-cc-pV5Z potential energy curves of the *gerade* (top) and *ungerade* (bottom) electronic states of N_2^+. The reference energy is taken as that of N_2 ($X^1\Sigma_g^+$, $v'' = 0$). The adiabatic ionization energy of N_2 is taken from Ref [74]. The lowest dissociation limit (L1 @ 24.2884 eV) is located as given in Ref [56]. L2 (@ 26.1874 eV) and L3 (@ 26.6724 eV) were located using the excitation energies of N^+ and N, respectively. The thick line corresponds to N_2^+ ground state PEC.

Section VI), it is especially the highly excited vibrational states of the $C^2\Sigma_u^+$ state that are coupled with the $3^2\Sigma_u^+$ since an important part of these vibrational wavefunctions is located in the region where the radial coupling

Table 1. Spectroscopic constants of the electronic states of N_2^+ investigated in the present work. We give the equilibrium distance (R_e in Å), vibrational constants (ω_e, $\omega_e x_e$, $\omega_e y_e$, in cm^{-1}) and the rotational constants (B_e, a_e, in cm^{-1}). T_0 (in eV) is the adiabatic excitation energy calculated as the difference between the energies of the minimum of the ground state and the minimum of the considered excited state including the zero point vibrational energy corrections.

State	Method	R_e	ω_e	$\omega_e x_e$	$\omega_e y_e$	B_e	a_e	T_0
$X^2\Sigma_g^+$	This work [a]	1.1186	2202	16.47	0.16	1.923	0.018	0
	Calc. [b]	1.126	2200	16.10	0.04	1.897	0.018	0
	Calc. [c]	1.1257	2140	16.7			0.012	0
	Calc. [d]	1.1696	2075					0
	Calc. [h]	1.1167	2207	16.62	0.03	1.930	0.018	0
	Calc. [i]	1.1191	2198	16.09		1.922	0.018	0
	Exp. [e]	1.1164	2207			1.931		0
	Exp. [j]		2207	16.25		1.931	0.018	0
$A^2\Pi_u$	This work [a]	1.1800	1926	15.29	0.007	1.728	0.019	1.16
	Calc. [f]	1.1870	1850					1.10
	Calc. [g]	1.1812	1903					1.13
	Calc. [h]	1.1750	1904	15.03	0.006	1.744	0.018	1.12
	Calc. [i]	1.1772	1900	14.96		1.735	0.018	1.14
	Exp. [e]	1.1749	1903	15.02		1.744	0.018	1.14
	Exp. [j]		1903	15.11		1.744	0.018	1.13
$B^2\Sigma_u^+$	This work [a]	1.0855	2487	23.51	2.10	2.042	0.024	3.23
	Calc. [f]	1.0834	2370					3.14
	Calc. [g]	1.0829	2442					3.20
	Calc. [h]	1.0748	2419	21.53	1.15	2.084	0.021	3.17
	Calc. [i]	1.0771	2406	23.37		2.074	0.020	3.15
	Exp. [e]	1.0742	2419	23.19	0.53	2.07456	0.024	3.16
	Exp. [j]		2421	24.07		2.083	0.021	3.15
$a^4\Sigma_u^+$	This work [a]	1.3467	1161	8.02	1.71	1.327	0.048	4.90
	Calc. [b]	1.353	1173	17.8		1.315	0.023	4.75
	Calc. [d]	1.42	1186					3.5
	Calc. [f]	1.3727	1080					4.61
	Calc. [h]	1.3482	1182	16.90	0.02	1.325	0.023	4.78
$D^2\Pi_g$	This work [a]	1.4802	973	12.2	0.05	1.098	0.016	6.56
	Calc. [c]	1.5235	772					6.26
	Calc. [d]	1.5494	968					5.90
	Calc. [h]	1.4705	909	11.9	0.03	1.1051	0.018	6.49
	Calc. [i]	1.4740	904	11.98		1.10473	0.019	6.47
	Exp. [e]	1.471	907	11.91	0.01	1.113	0.020	6.49
$C^2\Sigma_u^+$	This work [a]	1.2585	1984	10.38	0.36	1.519	0.017	8.06
	Calc. [f]	1.2717	1980					7.73
	Calc. [g]	1.2643	2044					7.95
	Calc. [h]	1.2531	2070		0.25	1.447	0.007	8.02
	Exp. [e]	1.2628	2071	9.29	0.43	1.509	89	8.01
$G^2\Sigma_g^+$	This work [a]	1.6901	923	25.04	8.12	0.881	0.002	10.07
	Calc. [h]	1.6318	883	24.51	7.89	0.896	0.001	9.82
$c^4\Delta_u$	This work [a]	1.3384	1326		0.07	1.343	0.026	6.34
	Calc. [b]	1.339	1258	17.5		1.341	0.021	6.23
	Calc. [d]	1.39	1302					5.7
	Calc. [f]	1.3585	1160					6.19
	Calc. [c]	1.3383	1258					6.24
	Calc. [h]	1.3355	1261	15.72	0.04	1.350	0.020	6.30
$d^4\Sigma_u^-$	This work [a]	1.3321	1296	16.27	0.12	1.356	0.024	7.24
	Calc. [b]	1.335						7.14
	Calc. [d]	1.38						6.6
	Calc. [h]	1.3320	1286	15.39	0.06	1.357	0.020	7.22
$1^4\Sigma_g^-$	This work [a]	1.7911	586	8.12	0.47	0.766	0.017	10.19
	Calc. [h]	1.7803	543	7.52	0.32	0.759	0.012	10.04
$1^2\Delta_u$	This work [a]	1.3670	1152	53.14	4.60	1.287	0.007	8.20
	Calc. [f]	1.3839	1095					7.98
	Calc. [g]	1.3785	1139					7.97

(*Continued*)

Table 1. (Continued).

State	Method	R_e	ω_e	$\omega_e x_e$	$\omega_e y_e$	B_e	α_e	T_0
$1^2\Sigma_u^-$	This work [a]	1.3491	1393	24.04	0.33	1.322	0.011	8.26
	Calc. [f]	1.3547	1208					8.04
	Calc. [g]	1.3489	1228					8.03
	Calc. [h]	1.3325	1309	28.23	2.03	1.353	0.002	8.09
$1^6\Sigma_u^+$	This work [a]	2.6622				0.339	0.362	8.93
$f^4\Pi_u$	This work [a]	1.1488	2148	23.15	0.06	1.823	0.041	9.43
Inner potential	Calc. [d]	1.19	2054					9.2
	Calc. [f]	1.1600	1986					9.44
	Calc. [c]	1.1580	2038					9.37
	Calc. [g]	1.1537	2104					9.40
	Calc. [h]	1.1515	2099	22.42	0.03	1.820	0.020	9.39
$f^4\Pi_u$	This work [a]	1.9925	413	12.35	2.74	0.606	0.025	8.39
Outer potential	Calc. [b]	2.008						8.19
	Calc. [d]	1.84	783					7.5
	Calc. [h]	2.0103	452	8.76	0.47	0.595	0.012	8.35
$b^4\Pi_g$	This work [a]	1.4389	1021	12.13	0.26	1.1562	0.019	5.86
	Calc. [h]	1.4483	1008	11.41	0.11	1.1477	0.017	5.75
$2^2\Pi_u$	This work [a]	1.8929	639	7.18	0.17	0.671	0.004	9.93
	Calc. [d]	1.7594	911					9.30
	Calc. [c]	1.8726	705					9.13
	Calc. [h]	1.8857	657	4.98	0.39	0.677	0.007	9.67
$2^4\Pi_u$	This work [a]	2.4106	399	3.22	2.09	0.414	0.019	10.36
	Calc. [h]	2.4278	353	2.94	0.27	0.408	0.004	10.29
$2^4\Sigma_u^-$	This work [a]	1.9897	532	14.55	3.38	0.60792	0.002	10.42
$1^2\Phi_u$	This work [a]	1.9661	599	21.07	1.20	0.62254	0.011	10.50
$1^2\Phi_g$	This work [a]	1.4663	1009	9.76	0.27	1.1304	0.02	7.66
	Calc. [h]	1.4606	997	9.80	0.15	1.1287	0.016	7.53
$3^2\Pi_u$	This work [a]	2.8691	302	7.94	0.05	0.29234	0.001	11.57
$3^2\Sigma_u^+$	This work [a]	3.1711	222	16.90	2.89	0.23995	0.012	11.81

a.MRCI/aug-cc-pV5Z.
b.MRCI/AVQZ. Ref [41].
c.MRDCI/6-311 +G(2d). Ref [57].
d.CI. Ref [58].
e.Ref [59].
f.MRDCI/6-311 +G(2d). Ref [57].
g.Extended Gaussian basis sets and large CASSCF/multireference CI wave functions/(13s 8p 6d 4f)/[4s 3p 2d 1f] ANO. Ref [67].
h.icMRCI+Q/56+CV+DK. Ref [60].
i.MRCI/aug-cc-pCV5Z. Ref [61].
j.Molecular constants have been measured using fast-ion-beam laser spectroscopy. Ref [62].

is large. The radial coupling between the $C^2\Sigma_u^+$ and $B^2\Sigma_u^+$ states is maximum around 2.46 bohr [43], close to the minimum of the $C^2\Sigma_u^+$ state where the energy gap at the avoided crossing is larger than in the $C^2\Sigma_u^+ - 3^2\Sigma_u^+$ interaction. It is noteworthy that the radial coupling overlap and that the two non-adiabatic interactions cannot be considered as separated two-by-two systems. Indeed, the three $^2\Sigma_u^+$ states strongly interact. The $1^2\Sigma_u^-$ and $2^4\Sigma_u^-$ states are crossing the $C^2\Sigma_u^+$ state and may couple together by spin-orbit (Figure 3(d)). The $^4\pi_u$ states are also crossing the $C^2\Sigma_u^+$ state, where spin-orbit conversions may occur (Figure 3(d)). These states are also mutually coupled vibronically (Figure 3(b)).

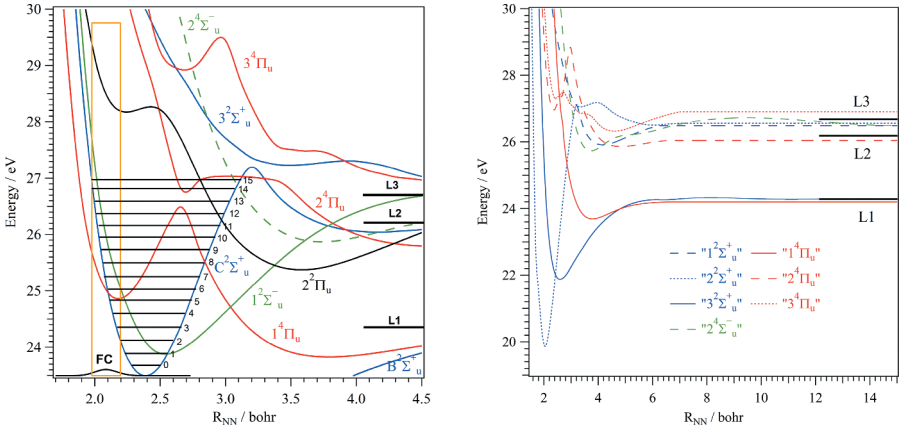

Figure 2. Adiabatic (left) and diabatic (right) PECs of the *ungerade* excited states of N_2^+ involved in the predissociation branching ratios calculations of the $N_2^+(C^2\Sigma_u^+)$ state. The reference energy is taken as that of $N_2(X^1\Sigma_g^+, v'' = 0)$. For obtaining the diabatic PECs from the adiabatic ones, we used the B – C radial coupling from Ref [43]. in addition to the couplings presented in Figure 3

IV. Radiative, predissociative, and natural lifetimes of the $N_2^+(C^2\Sigma_u^+, v^+)$ vibrational levels

The calculated potentials of Figure 2, spin-orbit couplings and dipole transition moments displayed in Figure 3, were incorporated into the LEVEL [64] and BCONT programs of Le Roy [65] to deduce the radiative and the spin–orbit-induced predissociation lifetimes of the vibrational levels of N_2^+.

The radiative lifetimes were deduced using the following formula

$$\tau^{rad,v^+} = \sum_{v''} \frac{1}{A_{v'^+v''^+}}$$

where $A_{v'^+v''^+}$ corresponds to the spontaneous emission Einstein coefficient from an ionic v'$^+$ level to a v"$^+$ level. This needs the transition moments between both initial and final electronic states as well as their potential energy curves. The data are given in Table 2. The validity of our approach was already noticed, for instance, for the SH $(A^2\Sigma^+)$ state through the direct comparison between our theoretical data and experimental measurements [66].

The $C^2\Sigma_u^+$ vibrational levels may decay radiatively to populate either the $X^2\Sigma_g^+$ or the $D^2\Pi_g$ states (Figure 1). The dipole moments of the C-X and C-D of these allowed transitions are given in Figure 3(c). Table 2 lists the radiative lifetimes of $N_2^+(C^2\Sigma_u^+, 0 \le v^+ \le 15)$ as computed using the LEVEL code [64]. For the $C^2\Sigma_u^+$–$X^2\Sigma_g^+$ radiative decays of the $0 \le v^+ \le 6$ levels, the corresponding radiative lifetimes are in a good agreement with the results deducted using the

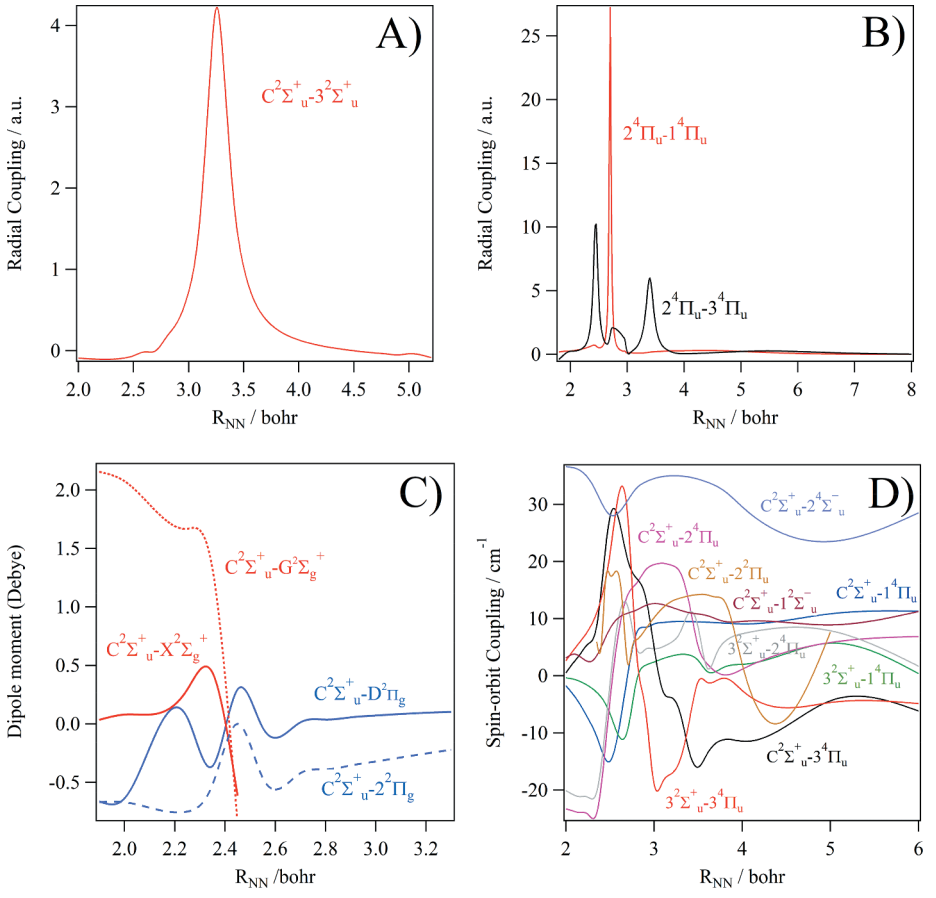

Figure 3. Radial couplings between the $^2\Sigma_u^+$ states (in A) and those between the $^4\pi_u$ states (in B). In C), we give the transition dipole moments between the $C^2\Sigma_u^+$ state and some electronic-excited states of N_2^+. In D), we plot the spin-orbit couplings between the electronic states depicted in Figure 2

empirical RKR potentials [67]. Again, this confirms the good quality of our *ab initio* PECs and dipole moments. When compared to previous experimental radiative lifetimes, a good agreement is found with those measured by Govers and coworkers and by Erman for $v^+ \leq 2$ (Table 2). Nevertheless, none of them gave an accurate estimation for $v^+ \geq 3$ since it is hard to deduce these quantities from experiments. Table 2 shows that the $C^2\Sigma_u^+$–$D^2\pi_g$ radiative decays affect the lifetimes of the upper levels of the C ($v^+ \geq 7$) states. It is worth noting that the lifetimes of the upper levels exhibit an irregular evolution, which may be related to the non-monotonic evolution of the corresponding transition dipole moments along the NN distance. Experimental measurements are welcomed for confirmation.

Table 2 gives also the predissociative lifetime obtained by three approaches. First, the lifetime is computed using the BCONT code [65]. We considered the C state spin-orbit-induced predissociation by the $1^4\pi_u$, 2^4

Table 2. Radiative ($\tau_{radiative}$), predissociative ($\tau_{predissociative}$) and natural ($\tau_{natural}$) lifetimes of the $N_2^+(C^2\Sigma_u^+, 0 \le v^+ \le 15)$ vibrational levels. All values are in ns. τ^{rad}_{C-X} and τ^{rad}_{C-D} correspond to the radiative lifetimes associated with the $C^2\Sigma_u^+$–$X^2\Sigma_g^+$ and $C^2\Sigma_u^+$–$D^2\pi_g$ transitions. τ^{rad}_{global} is the global radiative lifetime computed as $\frac{1}{\tau^{rad}_{global}} = \frac{1}{\tau^{rad}_{C-X}} + \frac{1}{\tau^{rad}_{C-D}}$. $\tau^{prediss}_{C-1}$, $\tau^{prediss}_{C-2}$ and $\tau^{prediss}_{C-3}$ correspond to the C state spin-orbit induced predissociation lifetimes by the $1^4\pi_u$, $2^4\pi_u$ and $2^4\Sigma^-_u$ states respectively. $\tau^{prediss}_{Cglobal,SO}$ is for the global predissociation lifetime computed as $\frac{1}{\tau^{prediss}_{global}} = \frac{1}{\tau^{prediss}_{C-1}} + \frac{1}{\tau^{prediss}_{C-2}} + \frac{1}{\tau^{prediss}_{C-3}}$. . $\tau^{prediss}_{C}$ is the predissociation lifetime estimated by the time-dependent method and $\tau^{prediss}_{C}$ is due to the coupling between the C and B states only . $\tau_{natural}$ is deduced as $\frac{1}{\tau_{natural}} = \frac{1}{\tau_{radiative}} + \frac{1}{\tau_{predissociative}}$.

	τ^{rad}_{C-X}						τ^{rad}_{C-D}	τ^{rad}_{global}	$\tau^{prediss}_{C-1}$	$\tau^{prediss}_{C-2}$	$\tau^{prediss}_{C-3}$	$\tau^{prediss}_{CglobalSO}$	$\tau^{prediss}_{C}$	$\tau^{prediss}_{C-B}$	
	Calc. [a]	Calc. [b]	Exp. [c]	Exp. [d]	Exp. [e]	Exp. [f]	Calc. [a]	Calc. [a]	Calc. [a]	Calc. [a]	Calc. [a]	Calc. [a]	Calc. [g]	Calc. [h]	$\tau_{natural}$ [a]
0	68.9	65.1	70.2	800	90		677	62.57							
1	62.9	62.6	66.6		90	77.0 ±3.0	607	57.01							
2	61.8	60.9	64.4		90	78.9 ±3.0	770	57.24							
3	60.7	59.5	62.9			4 ±1	729	56.04	28.7			28.7		7.19	18.97
4	59.2	58.5	62.1			5 ±1	783	55.03	0.585			0.585	1.67	2.46	0.573
5	62.9	57.9	62.1			5 ±1	151	44.40	2.29			2.29	1.29	1.62	2.278
6	62.2	57.5	62.6				311	51.83	1.75			1.75	1.94	1.08	1.692
7	69.9						13.4	11.24	0.0642			0.0642	2.52	0.74	0.063
8	71.6						9.18	8.13	0.0802			0.0802	0.71	0.51	0.079
9	71.3						7.83	7.15	0.0464			0.0464	0.38	0.36	0.046
10	70.6						7.16	6.50	0.341			0.341	0.98	0.29	0.324
11	20.4						80.4	16.27		$5360x10^9$		$5360x10^9$	0.32		16.26
12	10.08						81.5	8.98		$2.23x10^9$		$2.23x10^9$	0.24		8.97
13	68.3						80.3	36.91			449	449	0.31		34.01
14	176						80.9	55.42			5.16	5.16	0.21		4.72
15	71.18						7.11	6.46			978	978	0.0017		6.41

a.This work, Fermi Golden rule with spin-orbit channels.
b.CASSCF/MRCI computations where the valence orbitals are considered in the active space. Ref [67].
c.Derived using an RKR potential using available experimental data. Ref [67].
d.Ref [21].
e.Govers and co-workers. Refs. [24,25].
f.Erman [26] using high-resolution High Frequency Deflection technique.
g.This work, time-dependent method.
h.Fermi Golden rule with B state, Ref [43].

π_u and $2^4\Sigma^-_u$ states, respectively. Mainly, the predissociative $0 \leq v^+ \leq 10$ levels lifetimes are due to the $1^4\pi_u$ induced predissociation leading to L1. For the upper levels, the $2^4\pi_u$ and $2^4\Sigma^-_u$ states are in action populating thus L2 and L3. Nevertheless, the corresponding lifetimes are somehow too long to be a realistic, signature of another dynamics (cf. Section VI). Second, we extract a lifetime from the time evolution of the norm P(t) of the wave packet initially prepared in a vibrational level of the C state. By adding an absorbing complex potential in the asymptotic region in each electronic state, the decrease of the total norm is a signature of the dissociation through the different channels. Note that the decay is always non-exponential and the rate is estimated from the initial quasi linear part of ln(P(t)). Finally, we report the lifetimes computed by the Fermi Golden rule in Ref [43] by considering the interaction between the C and B states only. In summary, the first method focuses on the spin-orbit coupling and discards the strong non-adiabatic interaction while the third one discards both the spin-orbit and the important interaction with the $3^2\Sigma_u^+$ state, which has a strong influence on the dynamics. It is thus not surprising that the results may be rather different since the methods sometimes use a truncated electronic basis set. The complex dynamics in the complete basis set provides more oscillatory results, which could be explained by the possibility of trapping some components of the wave packet in the wells of the π states leading to a slower decay. Indeed, the expected behavior is more complex than a textbook coupling between a bound state and a continuum. Nevertheless, the comparison of these different results remains interesting since they may illustrate the relative role of the different processes. Still, the results given in Table 2 confirm the already established sudden drop of the natural lifetimes of the $N_2^+(C^2\Sigma_u^+, 3 \leq v^+ \leq 15)$ levels because of the dominance of the predissociation processes, which will be our focus on the following parts of this manuscript.

V. Present state-to-state N_2^+ ion unimolecular decomposition investigations

To complement previous work on the predissociation of $N_2^+(C^2\Sigma_u^+, v^+)$, we performed a combined experimental and first-principles treatment to fully investigate the state-to-state predissociation of the $N_2^+(C^2\Sigma_u^+, v^+)$ upon ejection of an electron from the neutral $N_2(X^1\Sigma_g^+, v" = 0)$. Thus, we recorded the state-to-state BRs for N_2^+ $(C^2\Sigma_u^+, v^+) \rightarrow$ L1/L2/L3 using the mass-selected kinetically analyzed ions formed after N_2 ionization by the VUV light delivered by the DESIRS beamline at the French SOLEIL synchrotron facility. Theoretically, we computed the corresponding BRs using time-independent and time-dependent approaches where the nuclear motions were treated on a newly computed set of the N_2^+ PECs possibly

involved in the C state predissociation and of their radial and/or spin-orbit couplings. In order to highlight the possible-specific contribution of the electronic states lying in close to the C state, we performed several computations, where we examined all the possible processes, and derived their involvement in the C state predissociation. Our data together with those obtained previously are used to shed light on the specific processes undergone by $N_2^+(C^2\Sigma_u^+, v^+)$ ions.

a. Experimental determination of the BRs

Experiments were performed at the French SOLEIL synchrotron facility, more specifically at the molecular beam endstation SAPHIRS [68] located at the VUV undulator-based beamline DESIRS [69]. Nitrogen gas was sourced from Air Liquide (N60 grade) and used without further purification to create a molecular beam by expanding half a bar of N_2 through a 30 μm nozzle. The resulting supersonic beam traversed a 1 mm skimmer before crossing the synchrotron light at the center of the DELICIOUS3 double imaging photoelectron photoion coincidence spectrometer [70]. In the context of the present study of state-selected fragmentation, our imaging-based set-up offers the unique opportunity to collect 100% of the emitted electrons allowing a very efficient measurement of electron/ion coincidences.

The photon energy was set at 27.2 eV with a 1.5 meV bandwidth, while the polarization axis was chosen so that it was contained in the detection plane. The electrons and ions produced were accelerated in opposite directions by a 90 V/cm electric field. The ions were analyzed and detected by a modified Wiley McLaren spectrometer to yield the three dimensional translational energy distribution with a resolution of 15%, while the electrons energy distribution was obtained from their velocity map image through an Abel inversion [71] with resolutions down to a few % for the fastest photoelectrons. The data is then organized through the coincidence scheme to yield kinetic energy correlation diagrams, from which dissociation limits can be observed and their relative branching ratios extracted. Note that the translational energy of the parent ion has been fitted to a Boltzmann energy distribution to obtain an estimate of the molecular beam temperature, 80 ± 10 K.

The results of the state-to-state dissociative single photon ionization of N_2 are given in Figure 4, which shows the intensity of the N^+ collected fragments with respect to the electron and ion kinetic energy. These intensities are shown in this figure from the vibrational level (v^+ =3) where the predissociation of the C state starts. From this image, obtained at the single photon energy of hv = 27.2 eV, the branching ratios leading to the three accessible dissociation limits can be obtained for each vibrational level.

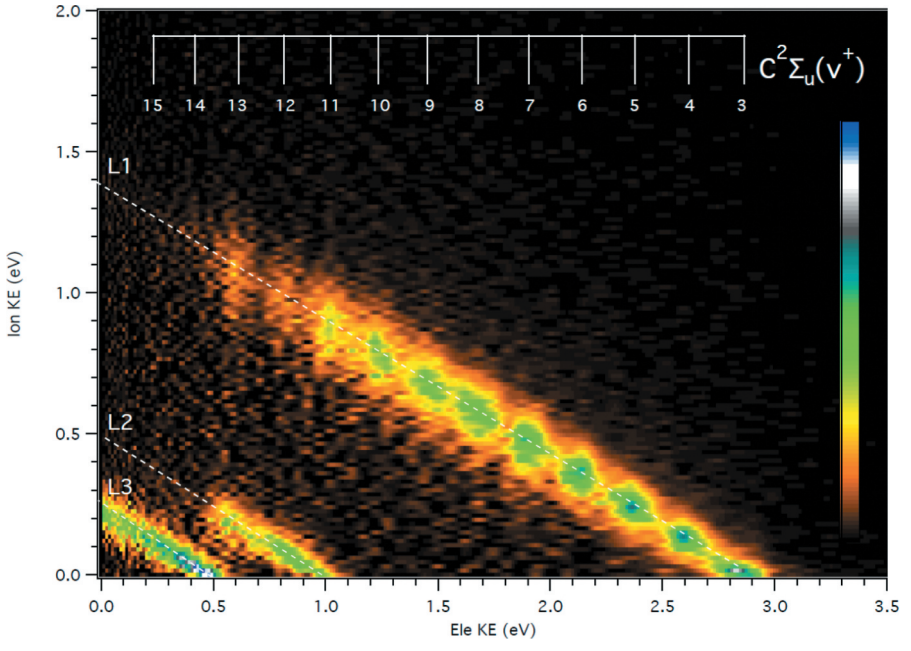

Figure 4. Intensity of dissociative ionization events yielding N^+ fragments recorded at a photon energy of 27.2 eV, as a function of electron kinetic energy (Ele KE) and N^+ kinetic energy. Diagonal white dashed lines point the three accessible dissociation limits, while the white vertical lines represent the expected position of the $N_2^+(C^2\Sigma_u^+)$ vibrational levels from $v^+ = 3$ until $v^+ = 15$, according to Yoshii *et al.* [75].

Figure 5 shows the kinetic energy distributions of the N^+ fragment for the vibrational levels $11 \leq v^+ \leq 15$ obtained through vertical projections of the matrix shown in Figure 4 centered at the electron kinetic energy corresponding to the vibrational levels, and using a width of ± 50 meV to obtain sufficient signal-to-noise, and the branching ratios to the first three limits of dissociation, which are also reported in Table 3. Note that for $3 \leq v^+ \leq 10$ levels, the only dissociation limit energetically available is L1, so that dissociation is 100% to this limit, as shown in Figure 6, while L2 and L3 open for $v^+ \geq 11$ and $v^+ \geq 13$, respectively.

The branching ratios have been extracted by fitting three Gaussian functions to the curves shown in Figure 5, one for each dissociation limit, and agree reasonably well with those deduced earlier by Nicolas *et al.* [28] using the TPEPICO technique. There are, however, some noticeable differences, especially for $v^+ \geq 14$, where our data show some signal in L2 and L1 (see Figure 5) – albeit with relatively high error bars due to the low signal-to-noise – whereas Nicolas *et al.* found 100% fragmentation to L3. Also, for $v^+ = 11$, they reported more fragmentation to the L2, while we find 74% and 26% BRs to L1 and L2, respectively, in

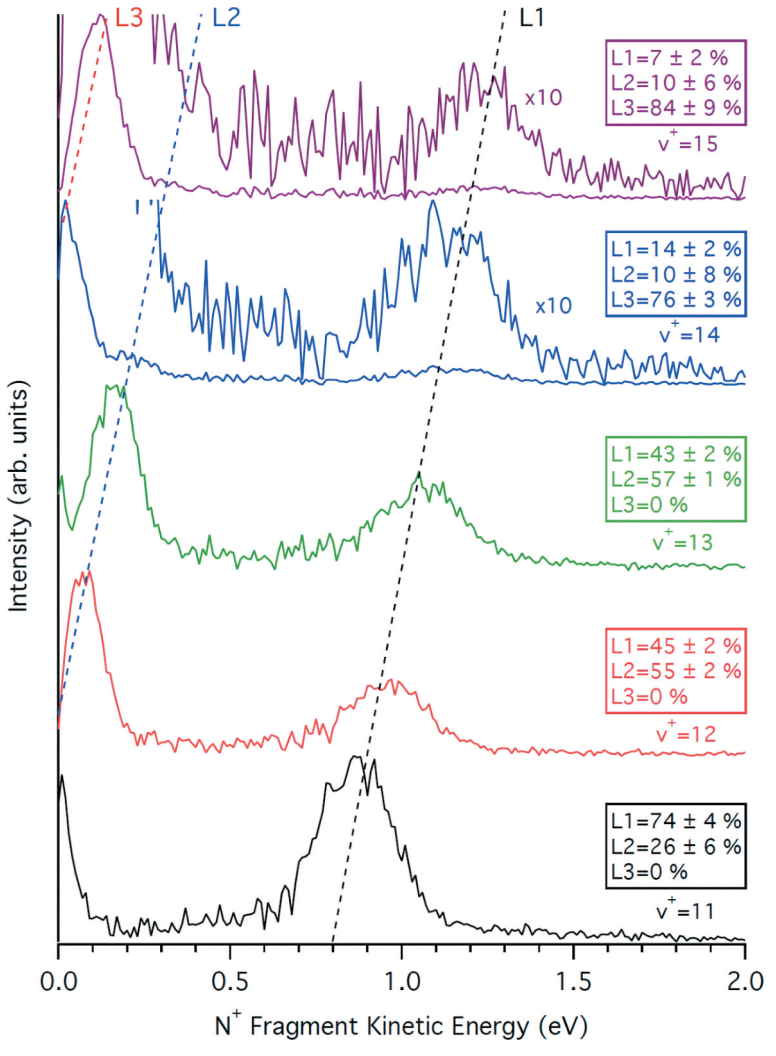

Figure 5. Kinetic energy release distributions of the N^+ fragment generated from N_2^+ ($C^2\Sigma_u^+$) v^+ =11 to 15, recorded at a fixed photon energy of 27.2 eV. The dashed diagonal lines show the three different dissociation limits available. For v^+ =14 and v^+ =15, the curves are also shown after multiplication by an order of magnitude to accentuate the weak dissociation to L2 and L1. The branching ratios to the three dissociation limits are provided for the five vibrational levels in Table 3.

better accordance with the present theoretical calculations that predict mainly dissociation to L1. These differences could be explained by the different experimental techniques and/or treatment methods, since our BRs are extracted from a single photon energy within a 100 meV electron binding energy bandwidth and the translational energy of the fragment ion is measured in 3D, while Nicolas *et al.* only had access to the 1D translational energy distribution, which accuracy might depend on the KER angular asymmetry, and performed a photon energy scan with

Table 3. Experimental and calculated branching ratios (in %) for the N_2^+ ($C^2\Sigma_u^+$, v^+) vibrational levels. The energies of the vibrational levels (E_v, in eV) are given with respect to N_2 ($X^1\Sigma_g^+$, $v'' = 0$). L_1, L_2 and L_3 refer to the first, second, and third dissociation limits as specified in Figure 1.

			Branching ratios																	
						Calc. [a]						Calc. [b]								
			exp.			d)			e)			d)			f)			g)		
Vib. Level	E_v		L_1	L_2	L_3	L_1	L_2	L_3	L_1	L_2	L_3	L_1	L_2	L_3	L_1	L_2	L_3	L_1	L_2	L_3
$3 \le v^+ \le 9$	-	This work	100.0	0.0	0.0	100.0	0.0	0.0	100.0	0.0	0.0	100.0	0.0	0.0	100.0	0.0	0.0	100.0	0.0	0.0
		Ref. [28] [c]	100	0	0															
$v^+ = 10$	25.961	This work	100.0	0.0	0.0	100.0	0.0	0.0	100.0	0.0	0.0	90.9	9.1	0.0	90.9	9.1	0.0	99.0	1.0	0.0
		Ref. [28] [c]	100	0	0															
$v^+ = 11$	26.174	This work	74 ±4	26 ±6	0.0	98.0	2.0	0.0	99.0	1.0	0.0	99.8	0.2	0.0	99.8	0.2	0.0	88.2	11.8	0.0
		Ref. [28] [c]	40	60	0															
$v^+ = 12$	26.382	This work	45 ±2	55 ±2	0.0	74.1	25.9	0.0	88.0	12.0	0.0	80.5	19.5	0.0	79.2	20.8	0.0	88.8	11.2	0.0
		Ref. [28] [c]	50	50	0															
$v^+ = 13$	26.583	This work	43 ±2	57 ±1	0	46.5	53.5	0.0	54.1	45.9	0.0	83.8	16.2	0.0	33.3	66.7	0.0	79.0	21.0	0.0
		Ref. [28] [c]	40	60																
$v^+ = 14$	26.778	This work	14 ±2	10 ±8	76 ±3	1.0	99.0	0.0	0.0	4.1	95.9	0.0	0.1	99.9	0.0	0.22	99.78	3.1	2.4	94.4
		Ref. [28] [c]	0.0	0.0	100.0															
$v^+ = 15$	26.966	This work	7 ±2	10 ±6	84 ±9	0.0	100.0	0.0	0.0	3.1	96.9	0.0	0.05	99.95	0.0	0.1	99.9	0.8	10.4	88.8
		Ref. [28] [c]	0.0	0.0	100.0															

a.Time-independent dynamical computations.
b.Time-dependent dynamical computations.
c.Threshold photoelectron-photoion coincidence spectroscopy.
d.Branching ratios calculated due to predissociation by the $1^4\Pi_u$, $2^4\Pi_u$ and $3^4\Pi_u$ states
e.Branching ratios calculated due to predissociation by the $1^4\Pi_u$, $2^4\Pi_u$, $D^2\Pi_u$ and $2^4\Sigma_u^-$ states
fBranching ratios calculated due to predissociation by the $3^2\Sigma_u^+$ $1^4\Pi_u$, $2^4\Pi_u$, $3^4\Pi_u$ and $2^4\Sigma_u^-$ states
gBranching ratios calculated due to predissociation by the $3^2\Sigma_u^+$ $B^2\Sigma_u^+ 1^4\Pi_u$, $2^4\Pi_u$, $3^4\Pi_u$ and $2^4\Sigma_u^-$ states

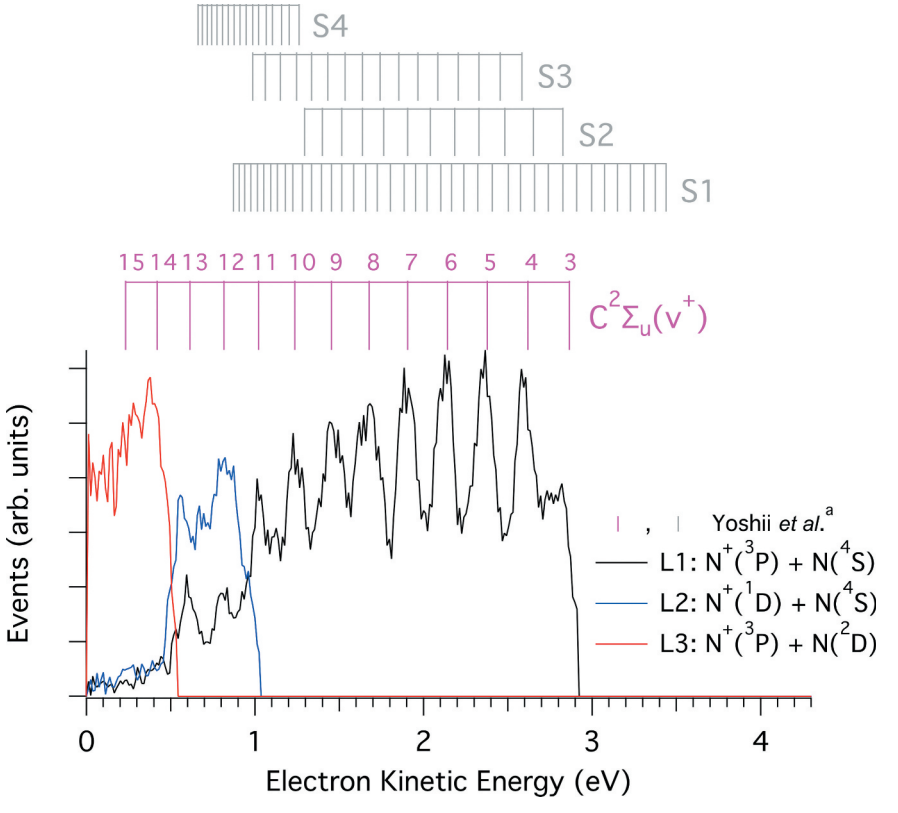

Figure 6. Number of dissociation events towards the three available limits, L1 (black), L2 (blue) and L3 (red), recorded at hv = 27.2 eV as a function of the electron kinetic energy. The relative intensity of the curves corresponds to the branching ratios to the three dissociation limits. The positions of the $N_2^+(C^2\Sigma_u^+)$ vibrational levels from Yoshii *et al.* [75] are marked in magenta, as well as four different progressions in gray S1($2^2\Pi_g$), S2($^2\Sigma_u^-$), S3($^2\Delta_u$) and S4($^2\Pi_u$) from the same reference.

a better electron resolution. It is well known that TPEPICO experiments can be affected by the presence of autoionization [72]. Nevertheless, our data show that dissociation to the L1 is gradually quenched by the opening of the L2 and L3 channels, but does not completely disappear, with L2 also dramatically decreasing with the opening of L3. Note however, that due to the experimental resolution the $v^+ = 11$ and perhaps $v^+ = 12$ branching ratios might be affected by the presence of the $^2\Pi_g$ progression, that could contribute up to 9% to these bands as reported by Baltzer *et al.* [73] Other progressions, reported only in threshold photoelectron spectra [36,74,75,76], could also contribute but since they were not seen in the high-resolution photoelectron spectrum by Baltzer *et al.*, they are dismissed in this work, although they are shown in Figure 6 for reference.

We have also recorded the TPEPICO curves of N_2^+ and N^+ in the photon energy region between 23.6 eV and 24.8 eV, i.e., below the $N_2^+(C^2\Sigma_u^+)$ v^+ =

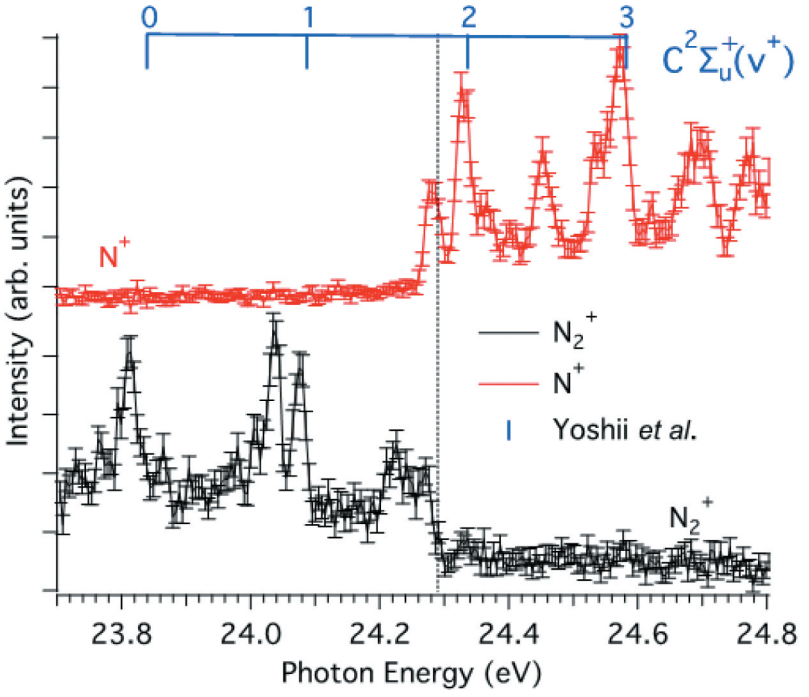

Figure 7. Threshold photoelectron photoion coincidence (TPEPICO) curves obtained for N^+ (red) and N_2^+ (black) by selecting only the photoionization events that correlate with the emission of a threshold electron. The threshold selection is achieved using the slow photoelectron method outlined by Poully *et al.* [77] and the parameters are set to deliver a total resolution of 15 meV. The vertical-dashed line represents the first dissociation limit towards $N^+(^3P) + N(^4S)$. Positions of the N_2^+ ($C^2\Sigma_u^+$) $0 \le v^+ \le 3$ vibrational levels are from Yoshii *et al.* [75].

5, and these are shown in Figure 7. These curves have also recently been acquired with a higher signal-to-noise over a larger energy range encompassing vibrational levels up to $v^+ = 6$, and discussed in great detail by Hrodmarsson *et al.* [36]. Therefore, they will not be further mentioned here, except to note that N_2^+ does not fully dissociate above $v^+ = 3$. Hrodmarsson *et al.* reported survival rates for the parent ion $^{14}N_2^+$ of a few % for $v^+ = 3$, 4, while for the $^{15}N_2^+$ isotope the survival gradually went from 37% at $v^+ = 3$, to 5% at $v^+ = 7$.

b. Theoretical determinations of the BRs

The $C^2\Sigma_u^+ \rightarrow 1^2\Sigma_u^-$ pathway can be ruled out since the respective spin-orbit integral is close to zero (Figure 3(d)). We considered the $C^2\Sigma_u^+$ state interacting, via spin-orbit, with only the $1^4\Pi_u$, $2^4\Pi_u$ and $3^4\Pi_u$ quartet states or after adding either the $2^4\Sigma^-_u$, the $1^2\Sigma^-_u$ or the $2^2\Pi_u$ states. Note that the $1^4\Pi_u$ state correlates adiabatically to L1, the $2^4\Pi_u$ and $2^4\Sigma_u^-$ states to L2, and the $1^2\Sigma_u^-$, $2^2\Pi_u$ and $3^4\Pi_u$ states to L3. We computed the state-to-state

predissociation BRs by considering each set of electronic states and their couplings using both a time-dependent and time-independent techniques to solve the nuclear motions. Within the time dependent treatment, the evolution of the $C^2\Sigma_u^+$ vibrational states is performed in the diabatic representation of the $B^2\Sigma_u^+$, $3^2\Sigma_u^+$, $2^4\Sigma_u^-$ and $^4\Pi_u$ states (Figure 2) together with the corresponding spin-orbit and their diabatic potential couplings. This allows us to observe possible vibronic predissociation mechanisms involving either the $^4\Pi_u$ states and/or the $^2\Sigma_u^+$ states, in addition to the spin-orbit one.

Predissociation and time-independent dynamics of $N_2^+(C^2\Sigma_u^+)$ ions

The predissociation branching ratios of the $C^2\Sigma_u^+$ state for the first 16 vibrational levels ($0 \leq v^+ \leq 15$) were calculated using the BCONT code [65]. BCONT allows the calculation of the isoenergetic predissociation from a discrete rovibrational level (v, J) of a bound potential energy curve to the continuum of a second dissociative state whose asymptote is situated below this level (v, J). These calculations consider the potential energy curves of the two electronic states and their spin-orbit couplings to deduce the predissociation lifetimes. For instance, the data introduced in this code are the potentials of the initial state $C^2\Sigma_u^+$ and those crossing this state and which are coupled to it by spin-orbit coupling. For each vibrational level, the percentage of connection (i.e. the BRs) was calculated as follows:

$$\%\mathrm{Lx} = \frac{I_{Lx}}{\sum I_{Lx}}$$

where x = 1, 2 or 3 and Lx = L1, L2 or L3 are the different dissociation limits and I_{Lx} are the transition intensities assigned to each dissociation limit for each vibrational level. The data are given in Table 3.

Time-dependent wavepacket dynamics of $N_2^+(C^2\Sigma_u^+)$ ions

Photodissociation dynamics is performed in the diabatic representation by taking as initial condition different vibrational eigenstates of the adiabatic $C^2\Sigma_u^+$ potential energy curve with average internuclear distance centered in the inner-well. The adiabatic-to-diabatic $\mathbf{D}(R)$transformation matrix is block diagonal with respect to Σ and Π subspaces. For each symmetry, the corresponding block is obtained by solving the coupled equations $\partial_R \mathbf{D}^{(\Sigma/\Pi)}(R) = \mathbf{F}^{(\Sigma/\Pi)}(R)\mathbf{D}^{(\Sigma/\Pi)}(R)$ where $\mathbf{F}^{(\Sigma/\Pi)}(R)$ is the matrix of the radial non-adiabatic coupling elements of the first derivative $\partial/\partial R$ in the Σ or Π manifold. Then, the full adiabatic potential energy matrix $\mathbf{V}^{adia}(R)$ containing the off-diagonal spin-orbit couplings between the Σ and Π states is transformed to the diabatic representation $\mathbf{V}^{dia}(R) = \mathbf{D}^T(R)\mathbf{V}^{adia}(R)\mathbf{D}(R)$. The propagation is carried out by the split operator algorithm [78] extended to the non-adiabatic case [79]. The kinetic energy operator is applied in the impulsion

and diabatic representation while the potential energy operator is expressed in the position and eigen basis set of the $\mathbf{V}^{adia}(R)$ matrix including the spin-orbit couplings. The computation uses a grid of 2^{13} points from R = 2 to 15 bohr. The time step is 1 a.u. (0.0241 fs). An optical potential is added at the boundary for R > 12 bohr to avoid unphysical reflection on the grid limit. This induces a decrease of the wavepacket norm as soon as some component in a given electronic state reaches the asymptotic region. The propagation is continued until the residual norm becomes constant when only trapped components survive. The branching ratios are then estimated from the partial photodissociation cross sections that are obtained from the Fourier transform $A_m^{v^+}(E) = \frac{1}{\sqrt{2\pi}}\int_0^{\infty} \chi_m^{v^+}(R_\infty, t)e^{iEt/\hbar}dt$ of each component $\chi_m^{v^+}(R_\infty, t)$ in electronic state m evolving from the initial vibrational state v^+ in the asymptotic region (here R_∞= 10 bohr). E is here the energy above the minimum of the $C^2\Sigma_u^+$ state. The partial cross-section is given by $\sigma_m^{v^+}(E) = \frac{4\pi^2\alpha a_0^2 k_m}{\mu} E\left|A_m^{v^+}(E)\right|^2$ where $\alpha = q^2/4\pi\varepsilon_0 hc$ is the fine structure constant, a_0 is the bohr radius, μ is the reduced mass and $k_m = \sqrt{2\mu(E-E_m)}/\hbar$ is the wave number in dissociative channel m with an asymptotic energy E_m [80,81].

In order to illustrate that the results strongly depend on the completeness of the electronic basis set, we compare the cross sections corresponding to the Franck-Condon initial wave packet, which is a weighted coherent superposition of all the vibrational states of the C state. The initial wave packet is the ground vibrational state of the ground electronic state promoted in the adiabatic C state (assuming a constant transition dipolar moment in the Condon approximation). In Figure 8, we compare the results obtained with the full basis set including the three $^2\Sigma_u^+$, three $^4\Pi_u$ and one $^4\Sigma_u^-$ states (panels (a) and (b)) with those given in a truncated basis containing only the three $^2\Sigma_u^+$ states (panels ((c) and (d)) or only the coupled $B^2\Sigma_u^+$- $C^2\Sigma_u^+$ as in Ref [43] (panels (e) and (f)). This minimum basis set overestimates the role of the B state as can be seen by comparing panels (f) and (d). Moreover, in the Franck-Condon case, the spin-orbit channel plays a significant role as shown in panel (b). Note that this example is a kind of average and the relative contribution in the dissociation towards L1 may depend on the initial vibrational state. These computations also reveal that both vibronic couplings and spin-orbit couplings are involved in the predissociation. The three $^2\Sigma_u^+$ states are strongly interacting by the radial couplings. Models truncating the basis to the couple $B^2\Sigma_u^+$- $C^2\Sigma_u^+$ or $C^2\Sigma_u^+$ – $3^2\Sigma_u^+$ are not sufficient.

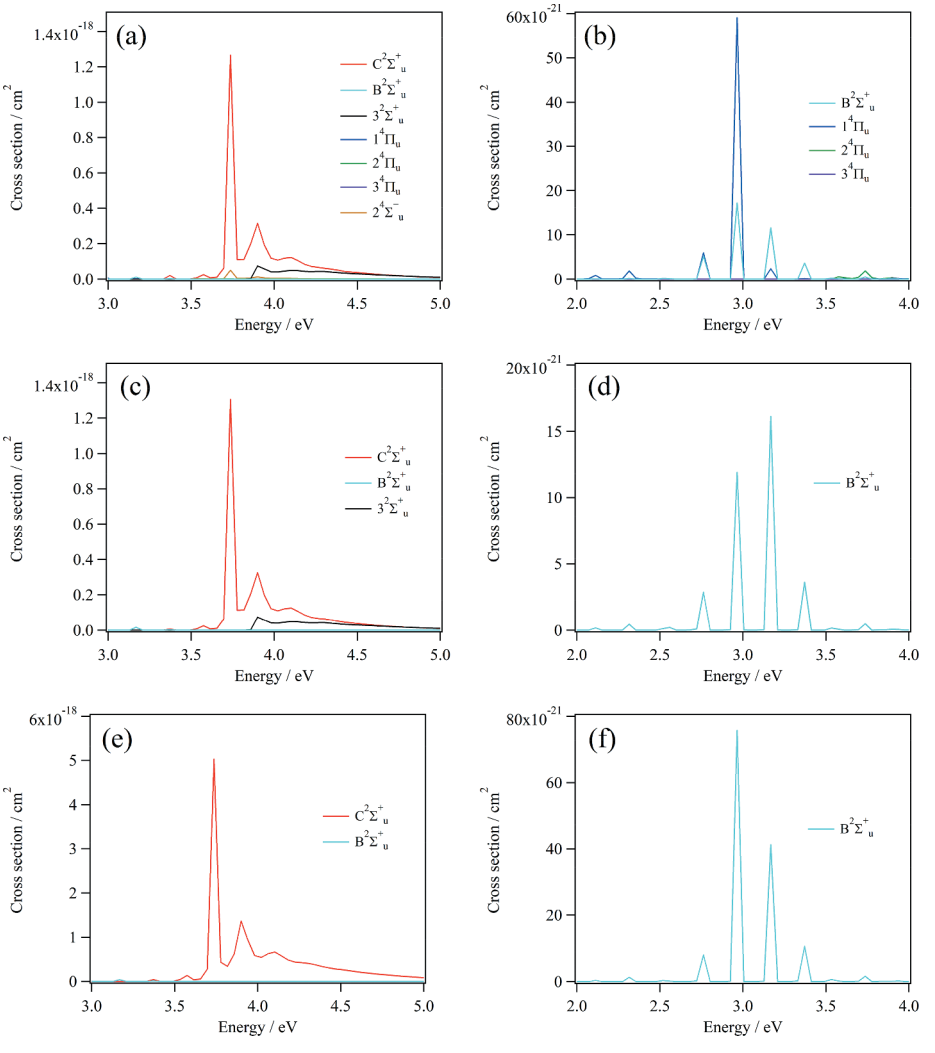

Figure 8. Photodissociation cross-sections of a Franck-Condon wave packet computed in three electronic basis sets. Panels (a) and (b): three $^2\Sigma_u^+$, three $^4\Pi_u$ and one $^4\Sigma_u^-$ states; panels (c) and (d): three $^2\Sigma_u^+$ states; panels (e) and (f): $B^2\Sigma_u^+$and $C^2\Sigma_u^+$ states only.

Results

The BRs are listed in Table 3. Although different BRs are obtained using these approaches, we should view them as complementary to fully understand the complex dynamics undertaken by the N_2^+ ions in the C levels. In any case, both theoretical approaches show that the C levels (i.e. $3 \leq v^+ \leq 10$), located in the energy range between L1 and L2, decay to populate L1, those between L2 and L3 (i.e. $11 \leq v^+ \leq 13$) lead to L1 and L2, whereas mainly L3 is reached through the decomposition of N_2^+ ($C^2\Sigma_u^+$, $v^+ = 14, 15$) ions. The $1^4\Pi_u$ and $2^4\Pi_u$ states are also crucial to explain the predissociation of the $v^+ \leq$

13 levels to form L1 and L2 species. For the N_2^+ ($C^2\Sigma_u^+$, $v^+ = 14, 15$) ions a supplementary channel leading specifically to L3 opens and leads to a different evolution partly due to shape resonances. This involves the electronic states correlating to this dissociation limit such as the $3^2\Sigma_u^+$, $3^4\Pi_u$, $D^2\Pi_u$ and $2^4\Sigma_u^-$ states. The influence of the $3^4\Pi_u$ state or the $D^2\Pi_u$ state is viewed however as negligible, and both are ruled out in the predissociation of the $N_2^+(C^2\Sigma_u^+)$ ions.

VI. The $N_2^+(C^2\Sigma_u^+)$ state full story

While the first principle computations are well-established accurate methodologies, Table 3 shows that none of these methods concord fully with the measured BRs for the C state predissociation. Nevertheless, we can consider them as complementary approaches to shed light on the complex and non-trivial mechanisms undergone by the $N_2^+(C^2\Sigma_u^+, v^+)$ ions. For the $v^+ \leq 10$ vibrational levels, the $C^2\Sigma^+_u$ state relaxes either by pre-dissociation to the first dissociation limit L1 or by fluorescence to the electronic ground state of N_2^+. That was proved by the present and previous experimental studies [19–30] and the branching ratios calculated in this work show that this is due to predissociation leading to L1 by vibronic interaction with the $B^2\Sigma_u^+$ and by spin-orbit coupling with $1^4\Pi_u$. The BR values estimated from the final population in the Π states are in a good agreement with those measured presently and the Nicolas *et al.* [28] ones. For $v^+ = 11$ and 12, the predissociation of the $C^2\Sigma^+_u$ state is distributed between the two first dissociation limits L1 and L2. Experimentally, we determined BRs of ~74% for L1 and ~26% for L2, while time-independent approach and time-dependent simulation without the $B^2\Sigma^+_u$ state lead to ~100% for L1. For the $v^+ = 12$ level, both theoretical percentages are distributed between the L1 and L2 limits with a predominance of L1. This is attributed mainly to the predissociation by the $1^4\Pi_u$ and $2^4\Pi_u$ states. The measured BRs for this vibrational level are however of ~50% for each limit. For $v^+ = 13$, we measure 41.7% to L1, 54.7% to L2 and a small percentage (~3.6%) for the third dissociation limit L3. These values are in close agreement with those computed here by the time-independent method taking into account the spin-orbit predissociation of the C state by the $^4\Pi_u$ and $2^4\Sigma_u^-$ states (Figure 2).

For the $v^+ = 14$ and $v^+ = 15$ vibrational levels, experimental measurements show a dissociation predominantly to the third limit with small contributions to L2 and L1, in very good agreement with our both theoretical predictions. The computations show that the spin-orbit coupling is less efficient here and that predissociation due to vibronic coupling is instead in action. Indeed, the spin-orbit couplings were not enough to change the calculated branching ratios.

The $N_2^+(C^2\Sigma_u^+)$ predissociative system is difficult to analyze by time-dependent methods because the profile of the potential energy curves of Σ and Π symmetry is favorable to trapping part of the wavepackets in the bound region leading to long lifetimes. Figure 9 gives the probability of occupying each adiabatic electronic state when the system is prepared in

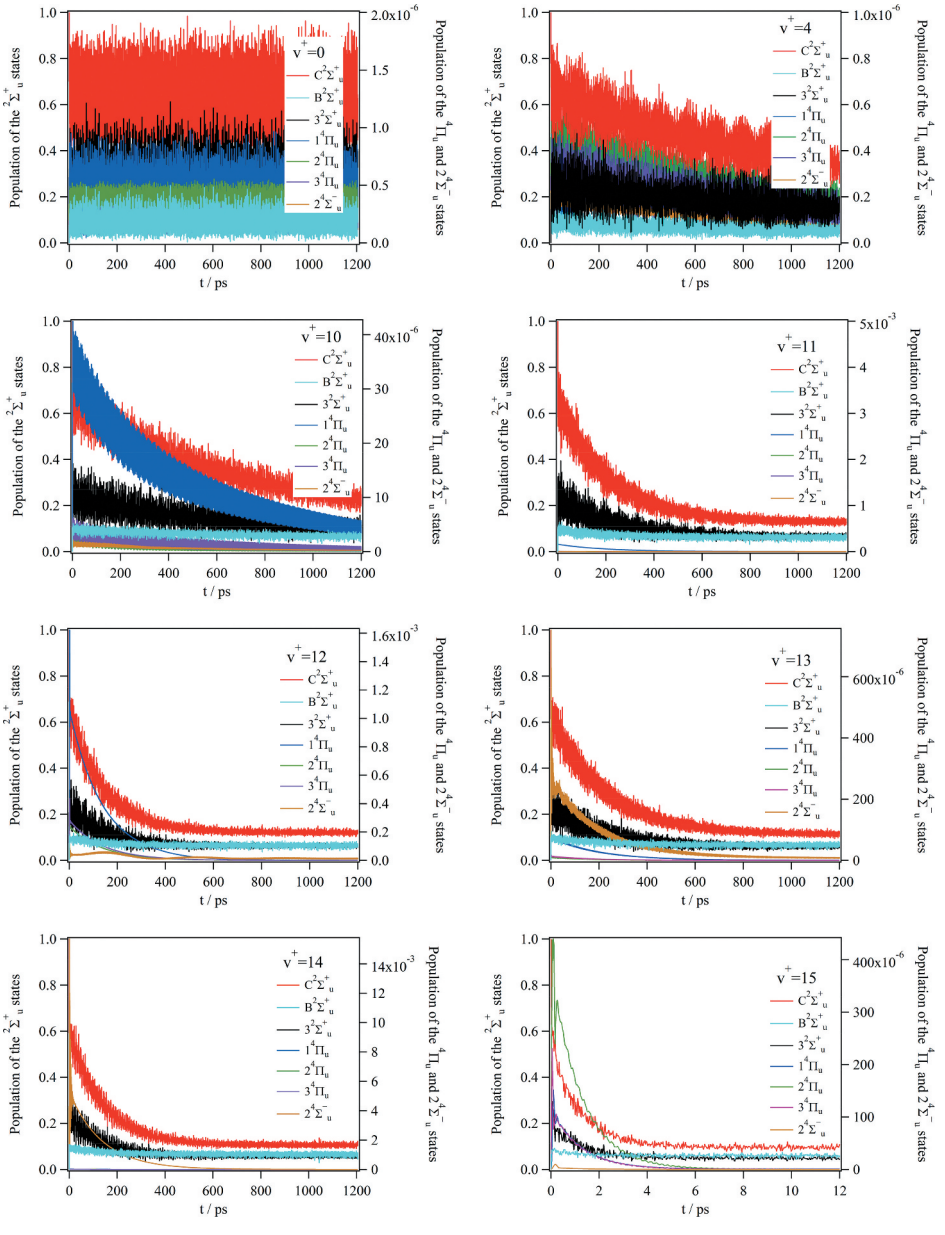

Figure 9. Time evolution of the wavepacket initially prepared in the $v^+ = 0$, 4, 10, 11, 12, 13, 14 and 15 vibrational levels of the $C^2\Sigma_u^+$ state of N_2^+ populating the $C^2\Sigma_u^+$, $B^2\Sigma_u^+$, $3^2\Sigma_u^+$, $1^4\Pi_u$, $2^4\Pi_u$, $3^4\Pi_u$ and $2^4\Sigma_u^-$ states. These evolutions are confirmed by longer dynamics (not shown). For $v^+ = 15$, the populations are almost those at t = 12 ps.

different vibrational states localized in the inner well of the $C^2\Sigma_u^+$. This reveals the early dynamics. The most remarkable observation is the very fast occupation of the three $C^2\Sigma_u^+$, $B^2\Sigma_u^+$ and $3^2\Sigma_u^+$ states due to the vibronic coupling for any initial state. The three states are populated directly during the first femtoseconds with slightly different weights with respect to v^+ and Rabi oscillations of weak amplitudes persist during the whole process. This non-adiabatic interaction is responsible of a part of the leakage towards L1 or L3. Spin-orbit coupling compete with this mechanism and allow the evolution towards the three L1, L2 and L3 asymptotes. The populations in the different states is not sufficient to extract the branching ratio among the dissociation channels due to the trapped components, which can decay by fluorescence only. Insight on the photodissociation is given by the time-dependent localization probability $\left|\chi_m^{v^+}(R_\infty, t)\right|^2$ at a large internuclear distance (R_∞= 10 bohr here) and more precisely by the integrated cross sections extracted from each component $\chi_m^{v^+}(R_\infty, t)$. The branching ratio (see Table 3) is obtained by summing the contribution coming from the correlated channels ($B^2\Sigma_u^+$ and $1^4\Pi_u$ for L1, $2^4\Pi_u$ and $2^4\Sigma_u^-$ for L2, $C^2\Sigma_u^+$, $3^2\Sigma_u^+$ and $3^4\Pi_u$ for L3). The decay towards the $B^2\Sigma_u^+$ by vibronic coupling confirms the contribution of this state in the predissociation via the L1 asymptote but it is not the only one since transition via the $1^4\Pi_u$ also occurs.

The second noteworthy point is the large branching ratio towards L3 and the fast decay of the $v^+ = 14$ and $v^+ = 15$ states. For $v^+ = 14$, the full decay requires ~600 ps. For $v^+ = 15$ level, the decay is even shorter and it needs ~6 ps. The difference of behavior is due to the shape of the vibrational initial states. As shown in Figure 10, the vibrational states with $v^+ < 14$ form a progression of successive bound states in the inner well of the C state (with $2 \leq \langle R_{NN} \rangle \leq 4$ bohr) while the $v^+ = 14$ and $v^+ = 15$ states are shape resonances near the top of the barrier. To illustrate this, Figure 10(a) gives the initial average interatomic distances of the eigenstates of the adiabatic C state. The states of the continuum are discretized by the diagonalization in a finite basis set. We clearly see the eigenstates that correspond to the inner well of the C state (with $2 \leq \langle R_{NN} \rangle \leq 4$ bohr) and those which correspond to the outer well (with $4 \leq \langle R_{NN} \rangle \leq 6$ bohr). We can see also the quasi continuum eigenstates where the value of the average distance ($\langle R_{NN} \rangle \geq 8$ bohr) is due to the finished grid used. Indeed, the fact that the average is large proves that these are discretized states of the continuum. Note that the parts located in the C state inner part potential are the only ones for which the Franck-Condon factors are large starting from $N_2(X^1\Sigma_g^+, v" = 0)$. Afterwards, the levels $v^+ = 14$ and $v^+ = 15$ are shape resonant states in the continuum of state $C^2\Sigma_u^+$ (Figure 9(e,f)) continuing the series of bound states in the inner-well. For the $v^+ = 14$ level, we see that, although the wavefunction part trapped in the inner-well of the C state exhibits 14 nodes,

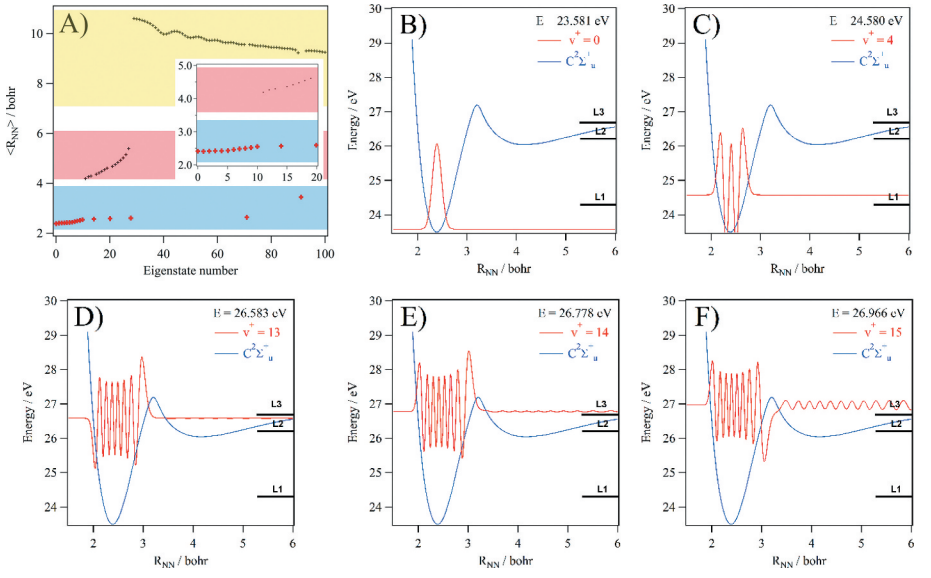

Figure 10. In A): Average position of the first 100 vibrational eigenstates of the $C^2\Sigma_u^+$ state with a discretization of the dissociation continuum. In the blue region, we give those located mainly in the inner potential well of the C state (i.e. $v^+ = 0–15$). The v^+ quantum number does not correspond to the eigenstate number for $v^+ > 10$ but continues the series of eigenstates located in the inner well with an increasing number of nodes. The $v^+ = 0–15$ levels are marked by red crosses. In the red region, those located in the outer potential well. In the yellow region, those delocalised in the continum (but artificially localized at long distance due to the finite grid). In the inset, we give an enlargement for the 20 first eigenstates where we can distinguish the $v^+ = 0 – 12$ eigenstates located in the inner potential well of the C state (red region). In B-F), we plot the vibrational wavefunctions of the $N_2^+(C^2\Sigma_u^+)$ state for $v^+ = 0$, 4, 13, 14 and 15, respectively. The energies of these levels with respect to the vibrationless N_2 ground state are also given. See text for more details.

noticeable oscillations in the dissociation continuum, *i.e.*, at long internuclear distances, are observed (Figure 10(e)). A similar discussion applies for the $v^+ = 15$ wavefunction (Figure 10(f)), where the area under these oscillations is even larger. These eigenvectors of the C adiabatic state are the only ones having a notable Franck-Condon factor above the L3 dissociation limit (note that Baltzer *et al.* [73] observe three more resonances above $v^+ = 15$). They are characterized by their localization inside the inner well and a weak amplitude beyond the barrier. All the neighboring eigenvectors have the opposite behavior with a large amplitude outside the barrier and a very weak amplitude in the well. This strong structuration of the eigenvectors is typical of a shape resonance due to tunneling. For instance, we clearly observe a strong variation of the shape of the eigenfunctions close to the barrier, which is typical of what is currently called a shape resonance due to a barrier. It is well-known that below and above the resonance energy the eigenvectors have a large amplitude in the outer region and a very weak amplitude inside the well while it is the contrary close to the resonance. As

this is an adiabatic view, this is not sufficient to describe the dissociation. The prompt direct population of the C asymptotic region by tunneling is only one of the processes that compete with vibronic and spin-orbit transition towards other electronic states. This direct tunneling component explains the faster decay of these states.

In sum, the dynamics for the upper C state vibrational levels was never fully described before by enlightening the competing role of vibronic couplings among the three $^2\Sigma_u^+$ states and spin-orbit interaction with the $2\Pi_u$ and $2^4\Sigma_u^-$ states. It is the first time that a resonance-induced dissociation is documented for dissociative photoionization.

VII. Conclusion

In addition to previous experimental and theoretical findings dynamics, we have combined direct state-of-the-art experimental measurements and high *ab initio* calculations to highlight the roles of the excited states of N_2^+ in the predissociation phenomena of the $C^2\Sigma_u^+$ state. The experiments consisted on the detection of the N^+ + N fragments formed after single photon ionization into state-selected vibrational states of N_2^+ and the deduction of the state-to-state branching ratios populating the three lowest dissociation limits of N_2^+ via the decomposition of the $N_2^+(C^2\Sigma_u^+)$ ions. These branching ratios were also computed using both time-dependent and time-independent complementary approaches where the nuclear motions were treated in a full new set of N_2^+ PECs lying close to the C state. The comparison of experimental data and those derived from these computations exposes the competing processes between vibronic couplings allowing dissociation towards L1 via the $B^2\Sigma_u^+$ state and the spin-orbit leading to the $^4\Pi_u$ states for the low levels, whereas a new mechanism was identified for the upper ones. Indeed, the $v^+ = 14, 15$ levels are identified as resonances, whose dissociation proceeds via vibronic coupling to the $3^2\Sigma_u^+$ state and spin-orbit coupling with the $D^2\Pi_u$ and $2^4\Sigma_u^-$ states forming directly and dominantly L3 products in good agreement with the experiments.

Although we treated the dissociative single photon ionization of a small (diatomic) molecule, the processes described here are complex. Our work showed that neither the time dependent nor the time independent theoretical approaches can give a complete vision on these complex dynamics undertaken after ionizing N_2. In sum, we showed that one needs an interplay between diverse computational and experimental investigations to disentangle the complex dynamics of the predissociation of the $N_2^+(C^2\Sigma_u^+)$, which was pointed out more than 60 years ago. This should help in the correct modeling of these important phenomena in atmospheric, planetary and plasma media. Similar complex situations can be found for other important molecular systems. For instance, the present findings may help to fully understand the isotopic effects

observed recently in the ultrafast dynamics of dissociative photoionization of N_2 and the unexpected branching ratios measured recently during the dissociation dynamics of N_2^+ induced by isolated attosecond XUV pulses in combination with few-optical-cycle near-infrared/visible (NIR/VIS) [30]. Similar approaches can be applied also to explain the isotopic effects in the VUV photodissociation of the N_2 and CO molecules [16,82] and that of larger molecular systems relevant for astrophysical, planetary, and atmospheric media and having environmental impacts such as HNCO [83].

Acknowledgments

We are indebted to the general technical staff of Synchrotron Soleil for running the facility. We would like also to thank Jean-François Gil for his technical help on the SAPHIRS molecular beam chamber, and Barbara Cunha de Miranda for her invaluable help in performing the experiments.

Disclosure statement

No potential conflict of interest was reported by the authors.

ORCID

M. Desouter-Lecomte http://orcid.org/0000-0002-6199-7401
G. A. Garcia http://orcid.org/0000-0003-2915-2553
L. Nahon http://orcid.org/0000-0001-9898-5693

References

[1] Feldman PD, Sahnow DJ, Kruk JW, et al. High-resolution FUV spectroscopy of the terrestrial day airglow with the far ultraviolet spectroscopic explorer. J Geophys Res Space Phys. 2001;106:8119.
[2] Owen TC. *On the origin of titan's atmosphere*. Planet Space Sci. 2000;48:747.
[3] Strobel DF, Shemansky DE. EUV emission from titans upper atmosphere voyager I encounter. J Geophys Res Space Phys. 1982;87:1361.
[4] Dutuit O, Carrasco N, Thissen R, et al. Critical review of N, N^+, N_2^+, N^{++}, and N_2^{++} main production processes and reactions of relevance to titan's atmosphere. Astrophys J Suppl S. 2013;204:20.
[5] Torr DG, Torr MR. Chemistry of the thermosphere and ionosphere. J Atmos Sol-Terr Phy. 1979;41:797.
[6] Torr MR, Torr DG. The role of metastable species in the thermosphere. Rev Geo Phys Space Phys. 1982;20:91.
[7] Teanby NA, Irwin PGJ, de Kok R, et al. Latitudinal variations of HCN, HC_3N and C_2N_2 in titan's stratosphere derived from cassini CIRS data. Icarus. 2006;181:243.
[8] Krasnopolsky VA. A photochemical model of titans atmosphere and ionosphere. Icarus. 2009;201:226.

[9] Peng Z, Gautier T, Carrasco N, et al. Titans atmosphere simulation experiment using continuum UV-VUV synchrotron radiation. J Geophys Res Planets. 2013;118:778.
[10] Balucani N. Elementary reactions of N atoms with hydrocarbons: first steps towards the formation of prebiotic N containing molecules in planetary atmospheres. Chem Soc Rev. 2012;41:5473.
[11] Knauth DC, Andersson BG, McCandliss SR, et al. The interstellar N_2 abundance towards HD 124314 from far-ultraviolet observations. Nature. 2004;429:636.
[12] Snow TP. Molecular nitrogen in space. Nature. 2004;429:615.
[13] Waite JH Jr., Young DT, Cravens TE, et al. The process of tholin formation in titan's upper atmosphere. Science. 2007;316:870.
[14] Thiemens MH, Chakraborty S, Dominguez G. The physical chemistry of mass-independent isotope effects and their observation in nature. Annu Rev Phys Chem. 2012;63:155–177.
[15] Meier RR, Samson JAR, Chung Y, et al. Production of N^+ from N_2 + hv: effective EUV emission yields from laboratory and dayglow data. Planet Space Sci. 1991;39:1197–1207.
[16] Song Y, Gao H, Chang YC, et al. Quantum-state dependence of product branching ratios in vacuum ultraviolet photodissociation of N_2. ApJ. 2016;819:23.
[17] Meier RR. Ultraviolet spectroscopy and remote sensing of the upper atmosphere. Space Sci Rev. 1991;58:1.
[18] Lie-Svendsen Ø, Rees MH, Stamnes K. Helium escape from the Earth's atmosphere: the charge exchange mechanism revisited. Planet Space Sci. 1992;40:1639–1662.
[19] Douglas AE. The near ultraviolet bands of N_2^+ and the dissociation energies of the N_2^+ and N_2 molecules. Can J Phys. 1952;30:302.
[20] Carroll K. The C-X system of N_2^+. Can J Phys. 1959;37:880.
[21] Wankenne H, Momigny J. Monomolecular and collision-induced predissociation in the mass spectrum of N_2^+. Int J Mass Spectrom Ion Phys. 1971;7:227.
[22] Wankenne H, Bolduc E, Marmet P. Ionisation dissociative de N_2. Can J Phys. 1975;53:770.
[23] Fournier P, Ozenne J-B, Durup J. Vibrational structure of predissociating molecular states: velocity spectrum of N^+ fragments from fast N_2^+ ions. J Chem Phys. 1970;53:4095.
[24] Fournier P, van de Runstraat CA, Govers TR, et al. Collision-induced dissociation of 10 keV N_2^+ ions: evidence for predissociation of the $C^2\Sigma_u^+$ state. Chem Phys Lett. 1971;9:426.
[25] Van de Runstraat CA, de Heer FJ, Govers TR. Excitation and decay of the $C^2\Sigma_u^+$ state of N_2^+ in the case of electron impact on N_2. Chem Phys. 1974;3:431.
[26] Erman P. Direct Measurement of the N_2^+ C state predissociation probability. Phys Scr. 1976;14:51.
[27] Asbrink L, Fridh C. The C state of N_2^+, studied by photoelectron spectroscopy. Phys Scr. 1974;9:338.
[28] Nicolas C, Alcaraz C, Thissen R, et al. Dissociative photoionization of N_2 in the 24–32 eV photon energy range. J Phys B: At Mol Opt Phys. 2003;36:2239.
[29] Aoto T, Ito K, Hikosaka Y, et al. Inner-valence states of N_2^+ and the dissociation dynamics studied by threshold photoelectron spectroscopy and configuration interaction calculation. J Chem Phys. 2006;124:234306.
[30] Trabattoni A, Klinker M, González-Vázquez J, et al. Mapping the dissociative ionization dynamics of molecular nitrogen with attosecond time resolution. Phys Rev X. 2015;5:041053.

[31] Eckstein M, Yang C-H, Kubin M, et al. Dynamics of N_2 dissociation upon inner-valence ionization by wavelength-selected XUV pulses. J Phys Chem Lett. 2015;6:419.
[32] Govers TR, van de Runstraat CA, de Heer FJ. Isotope effects in the predissociation of the $C^2\Sigma_u^+$ state of N_2^+. J Phys B. 1973;6:73.
[33] Govers TR, Fehsenfeld FC, Albritton DL, et al. Molecular isotope effects in the thermal-energy charge exchange between He^+ and N_2. Chem Phys Lett. 1974;26:134.
[34] Govers TR, van de Runstraat CA, de Heer FJ. Excitation and decay of the $C^2\Sigma_u^+$ state of N_2^+ following collisions of He^+ ions with N_2 isotopes. Chem Phys. 1975;9:285.
[35] Fournier PG, Govers TR, van de Runstraat CA, et al. Translational spectroscopy of the unimolecular dissociation $N_2^+ \rightarrow N^+ + N$. J Phys. 1972;33:755.
[36] Hrodmarsson HR, Thissen R, Dowek D, et al. Isotope effects in the predissociation of excited states of N_2^+ produced by photoionization of $^{14}N_2$ and $^{15}N_2$ at energies between 24.2 and 25.6 eV. Front Chem. 2019;7:222.
[37] Lorquet AJ, Lorquet JC. Isotopic effects in accidental predissociation, The case of the $C^2\Sigma_u^+$ state of N_2^+. Chem Phys Lett. 1974;26:138.
[38] Lorquet JC, Desouter M. Excited states of gaseous ions. Transition to and predissociation of the $C^2\Sigma_u^+$ state of N_2^+. Chem Phys Lett. 1972;16:136.
[39] Tellinghuisen J, Albritton DL. Predissociation of the $C^2\Sigma_u^+$ state of N_2^+. Chem Phys Lett. 1975;31:91.
[40] Roche AL, Lefebvre-Brion H. Some ab initio calculations related to the predissociation of the $C^2\Sigma_u^+$ state of N_2^+. Chem Phys Lett. 1975;32:155.
[41] Hochlaf M, Chambaud G, Rosmus P. Quartet states in the N_2^+ radical cation. J Phys B: At Mol Opt Phys. 1997;30:4509.
[42] Hochlaf M, Chambaud G, Rosmus P. CORRIGENDUM: quartet states in the N_2^+ radical cation. J Phys B: At Mol Opt Phys. 1998;31:4059.
[43] Paulus B, Pérez-Torres JF, Stemmle C. Time-dependent description of the predissociation of N_2^+ in the $C^2\Sigma_u^+$ state. Phys Rev A. 2016;94:053423.
[44] Roche AL, Tellinghuisen J. Predissociation and perturbations in the $C^2\Sigma_u^+$ state of N_2^+ from interaction with the $B^2\Sigma_u^+$ state. Mol Phys. 1979;38:129.
[45] Werner H-J, Knowles PJ et al.MOLPRO version 2015, a package of ab initio programs. 10/09/2020. Available from: http://www.molpro.net
[46] Knowles PJ, Werner H-J. An efficient second-order MC SCF method for long configuration expansions. Chem Phys Lett. 1985;115:259.
[47] Werner H-J, Knowles PJ. A second order multiconfiguration SCF procedure with optimum convergence. J Chem Phys. 1985;82:5053.
[48] Werner H-J, Knowles PJ. An efficient internally contracted multiconfiguration–reference configuration interaction method. J Chem Phys. 1988;89:5803.
[49] Knowles PJ, Werner H-J. An efficient method for the evaluation of coupling coefficients in configuration interaction calculations. Chem Phys Lett. 1988;145:514.
[50] Shamasundar KR, Knizia G, Werner H-J. A new internally contracted multi-reference configuration interaction method. J Chem Phys. 2011;135:054101.
[51] Dunning TH Jr. Gaussian basis sets for use in correlated molecular calculations. I. The atoms boron through neon and hydrogen. J Chem Phys. 1989;90:1007.
[52] Kendall RA, Dunning TH, Harrison RJ. Electron affinities of the first-row atoms revisited: systematic basis sets and wave functions. J Chem Phys. 1992;96:6796.
[53] Spelsberg D, Meyer W. Dipole-allowed excited states of N_2: potential energy curves, vibrational analysis, and absorption intensities. J Chem Phys. 2001;115:6438.
[54] Hochlaf M, Ndome H, Hammoutène D, et al. Valence–Rydberg electronic states of N_2 : spectroscopy and spin–orbit couplings. J Phys B. 2010;43:245101.

[55] Berning A, Schweizer M, Werner H-J, et al. Spin-orbit matrix elements for internally contracted multireference configuration interaction wavefunction. Mol Phys. 2000;98:1823.
[56] Tang X, Hou Y, Ng CY, et al. Pulsed field-ionization photoelectron-photoion coincidence study of the process $N_2+h\nu \rightarrow N^+ + N^+ + e^-$: bond dissociation energies of N_2 and N_2^+. J Chem Phys. 2005;123:074330.
[57] Bruna PJ, Grein F. The $X^2\Sigma_g^+$ and $B^2\Sigma_u^+$ states of N_2^+: hyperfine and nuclear quadrupole coupling constants, electric quadrupole moments, and electron-spin g-factors. A theoretical study. J Mol Spectrosc. 2004;227:67.
[58] Thulstrup EW, Andersen A. Configuration interaction studies of bound, low-lying states of N_2^-, N_2, N_2^+ and N_2^{2+}. J Phys B. 1975;8:965.
[59] Access date: 10/09/2020. Available from: http://Webbook.nist.gov
[60] Liu H, Shi D, Wang S, et al. Theoretical spectroscopic calculations on the 25 Λ–S and 66 Ω states of cation in the gas phase including the spin–orbit coupling effect. J Quant Spectrosc Radiat Transf. 2014;147:207.
[61] Shi D, Xing W, Sun J, et al. Spectroscopic constants and molecular properties of $X^2\Sigma_g^+$, $A^2\Pi_u$, $B^2\Sigma_u^+$ and $D^2\Pi_g$ electronic states of the N_2^+ ion. Comput Theor Chem. 2011;966:44.
[62] Scholl TJ, Holt RA, Rosner SD. Fine and Hyperfine Structure in $^{14}N_2^+$: the $B^2\Sigma^+_u$-$X^2\Sigma^+_g(0,0)$ Band. J Mol Spectrosc. 1998;192:424.
[63] Cooley JW. An improved eigenvalue corrector formula for solving the schrödinger equation for central fields. Math Comput. 1961;15:363.
[64] Le Roy RJ, *LEVEL 7.2, Chemical Physics Research Report No. CP-642, U. Waterloo*; 2002.
[65] Le Roy RJ, *BCONT, Chemical Physics Research Report No. CP-329R3, U. Waterloo*; 1993.
[66] Brites V, Hammoutène D, Hochlaf M. Accurate ab initio spin–orbit predissociation lifetimes of the A states of SH and SH^+. J Phys B: At Mol Opt Phys. 2008;41:045101.
[67] Langhoff SR, Bauschlicher CW Jr. Theoretical study of the first and second negative systems of N_2^+. J Chem Phys. 1988;88:329.
[68] Richard-Viard M, Delboulbe A, Vervloet M. Experimental study of the dissociation of selected internal energy ions produced in low quantities: application to N_2O^+ ions in the Franck-Condon gap and to small ionic water clusters. Chem Phys. 1996;209:159.
[69] Nahon L, de Oliveira N, Garcia G, et al. DESIRS: a state-of-the-art VUV beamline featuring high resolution and variable polarization for spectroscopy and dichroism at SOLEIL. J Synchrotron Rad. 2012;19:508.
[70] Garcia GA, De Miranda BKC, Tia M, et al. DELICIOUS III: A multipurpose double imaging particle coincidence spectrometer for gas phase vacuum ultraviolet photodynamics studies. Rev Sci Instrum. 2013;84:053112.
[71] Garcia GA, Nahon L, Powis I. Two-dimensional charged particle image inversion using a polar basis function expansion. Rev Sci Instrum. 2004;75:4989.
[72] Baer T, Guyon PM. An historical introduction to threshold photoionization. In: Baer T, Ng CY, Powis I, editors. High resolution laser photoionization and photoelectron studies. Chichester: John Wiley & Sons Ltd; 1995. p. 1.
[73] Baltzer P, Larsson M, Karlsson L, et al. Inner-valence states of N_2^+ studied by uv photoelectron spectroscopy and configuration-interaction calculations. Phys Rev A. 1992;46:5545.
[74] Merkt F, Softley TP. Rotationally resolved zero-kinetic-energy photoelectron spectrum of nitrogen. Phys Rev A. 1992;46:302.

[75] Yoshii H, Tanaka T, Morioka Y, et al. New N_2^+ electronic states in the region of 23-28 eV. J Mol Spectrosc. 1997;186:155.
[76] Yencha AJ, Ellis K, King GC. High-resolution threshold photoelectron and photoion spectroscopy of molecular nitrogen in the 15.0–52.7 eV photon energy range. J Electron Spectrosc Relat Phenom. 2014;195:160.
[77] Poully JC, Schermann JP, Nieuwjaer N, et al. Photoionization of 2-pyridone and 2-hydroxypyridine. Phys Chem Chem Phys. 2010;12:3566.
[78] Feit MD, Fleck JA, Steiger A. Solution of the Schrödinger equation by a spectral method. J Comput Phys. 1982;47:412.
[79] Alvarellos J, Metiu H. The evolution of the wave function in a curve crossing problem computed by a fast Fourier transform method. J Chem Phys. 1988;88:4957.
[80] Balint-Kurti GG, Dixon RN, Marston CC. Time-dependent quantum dynamics of molecular photofragmentation processes. J Chem Soc Faraday Trans. 1990;86:1741.
[81] Sodoga K, Loreau J, Lauvergnat D, et al. Photodissociation of the HeH^+ ion into excited fragments (n=2,3) by time-dependent methods. Phys Rev A. 2009;80:033417.
[82] Jiang P, Chi X, Zhu Q, et al. Strong and selective isotope effect in the vacuum ultraviolet photodissociation branching ratios of carbon monoxide. Nat Commun. 2019;10:3175.
[83] Bonnet L, Linguerri R, Hochlaf M, et al. Full-dimensional theory of pair-correlated HNCO photofragmentation. J Phys Chem Lett. 2017;8:2420.